Ore Geology Reviews 129 (2021) 103941

Contents lists available at ScienceDirect

Ore Geology Reviews

journal homepage: www.elsevier.com/locate/oregeorev

Origin of the carbonate-hosted Danaopo Zn-Pb deposit in western Hunan Province, China: Geology and *in-situ* mineral S-Pb isotope constraints

Tao Wu [a,b], Zhilong Huang [a,*], Lin Ye [a], Chen Wei [a,b], Jun Chen [a], Mu Yang [c], Zaifei Yan [a], Zhiheng Sui [d]

[a] State Key Laboratory of Ore Deposit Geochemistry, Institute of Geochemistry, Chinese Academy of Sciences, Guiyang 550081, China
[b] University of Chinese Academy of Sciences, Beijing 100049, China
[c] School of Geoscience and Info-Physics, Central South University, Changsha 410083, China
[d] Team 405, Bureau of Geology and Mineral Exploration and Development of Hunan Province, Jishou 416099, China

ARTICLE INFO

Keywords:
In situ S-Pb isotopes
Danaopo Zn-Pb deposit
Ore-material source
Reef limestone
Western Hunan-Eastern Guizhou (WHEG) metallogenic belt

ABSTRACT

The western Hunan-eastern Guizhou (WHEG) Pb-Zn metallogenic belt hosts around 300 carbonate-hosted Pb-Zn deposits (total Pb-Zn metal reserve: >20 Mt), accounting for a major proportion of Pb-Zn resource in China. The origin and ore-forming process of these Pb-Zn deposits are still under debate. The newly-discovered Danaopo Zn-Pb deposit (~150 Mt ore @ 2.58% Zn and 0.48% Pb), which was formed during the Early Devonian orogenic event (~410 Ma), is one of the largest Zn-Pb deposits in the region. In this study, LA-MC-ICP-MS S-Pb isotope analyses were performed on sulfides (pyrite, sphalerite, and galena) and sulfate (barite) from the Danaopo Zn-Pb deposit. $\delta^{34}S_{VCDT}$ values of the diagenetic and late hydrothermal barites are of +36.5 to +36.9‰ and +27.1 to +28.1‰, respectively. The sulfides $\delta^{34}S_{VCDT}$ values (+23.5 to +35.5‰) imply a thermochemical sulfate reduction (TSR) origin from coeval seawater sulfates, as supported also by the dissolution cavities of diagenetic barite and the nodular and stripe-textured calcite. Furthermore, *in-situ* sulfide Pb isotopic ratios of different ore-forming stages and altitudes are highly similar: $^{206}Pb/^{204}Pb$ = 18.144–18.254, $^{207}Pb/^{204}Pb$ = 15.718–15.797, and $^{208}Pb/^{204}Pb$ = 38.378–38.605. Such narrow Pb isotopic ranges suggest well-mixing of multiple Pb sources, which likely include the Lower Cambrian Niutitang Fm. (LCNF) black shale, Proterozoic Banxi Group metamorphic basement rocks, and the Lower Cambrian Qingxudong Fm. (LCQF) reef limestone. Considering the deposit geological and S-Pb isotopic features, we suggest that the hydrothermal fluids may have circulated and extracted metals from various sequences in the basin. The fluids then ascended along the Huayuan-Zhangjiajie fault zone and mixed with reduced sulfur-bearing fluids from ore-bearing strata and precipitated the sulfide ores. Mineralization at the Danaopo deposit is thus best classified as Mississippi Valley Type (MVT), which is controlled by the ore-hosting reef limestone and various fault structures.

1. Introduction

Lead-zinc (Pb-Zn) mineralization of the western Hunan-eastern Guizhou (WHEG) metallogenic belt is hosted in the platform carbonate sequences in southeastern Yangtze Block (Figs. 1 and 2; Yang and Lao, 2007). The WHEG metallogenic belt contains about 300 Pb-Zn deposits with over 20.0 million tonnes (Mt) of Pb and Zn reserve (Zhao et al., 2016; Li, 2018). These Pb-Zn deposits are characterized by: (1) large tonnage of low ore-grade ore (avg. 4% Pb + Zn; Wei et al., 2020), with simple ore mineralogy and thus low cost for mining and mineral processing (Hu et al., 2017; Tan et al., 2018); (2) stratiform and lenticular orebodies hosted mostly in the Lower Cambrian Qingxudong Fm. (LCQF) carbonate rocks; (3) orebody distributions controlled by algal reef zone and regional deep faults (Tang et al., 2013; Zhao et al., 2016); (4) low–medium temperatures (140–220 °C) and medium–high salinities (11.0–19.0 wt% NaCl equiv.) of the ore-forming fluids (Liu et al., 1999a; Cai et al., 2014; Duan et al., 2014; Wei, 2017); (5) presence of bitumen with sulfides and methane in fluid inclusions, suggesting organic matter involvement during the ore formation (Liu et al., 1999b; Zhou et al., 2014).

* Corresponding author.
E-mail addresses: wutao@mail.gyig.ac.cn (T. Wu), huangzhilong@vip.gyig.ac.cn (Z. Huang), Yelin@vip.gyig.ac.cn (L. Ye), weichen@mail.gyig.ac.cn (C. Wei), chenjun@mail.gyig.ac.cn (J. Chen), yangmu@csu.edu.cn (M. Yang), yanzaifei@mail.gyig.ac.cn (Z. Yan).

https://doi.org/10.1016/j.oregeorev.2020.103941
Received 24 October 2020; Received in revised form 10 December 2020; Accepted 13 December 2020
Available online 16 December 2020

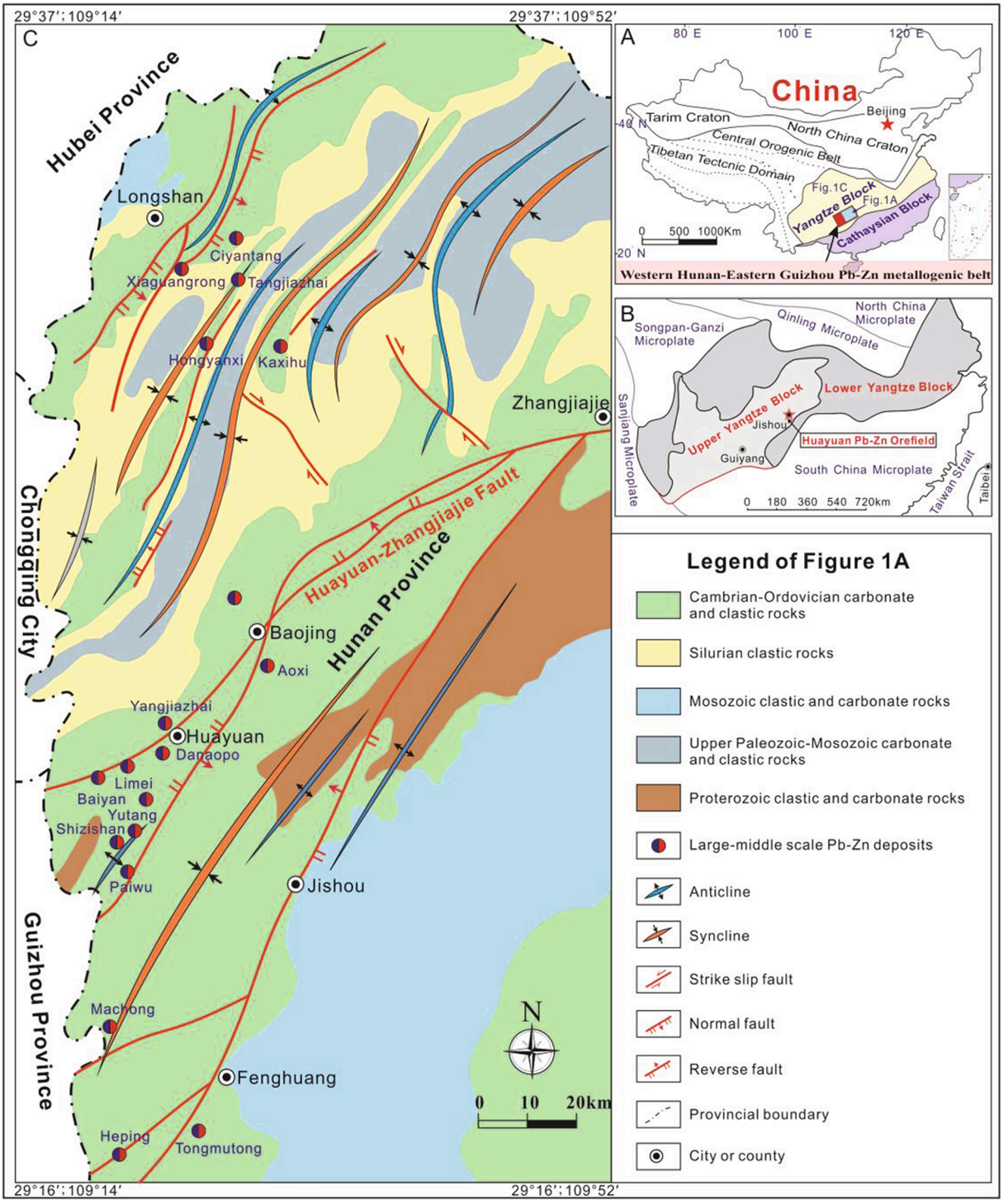

Fig. 1. (A) Regional tectonic setting of the western Hunan-eastern Guizhou Pb-Zn metallogenic belt (modified after Zhou et al., 2013; Li, 2018); (B) Geotectonic setting of the Huayuan Pb-Zn orefield in the Upper Yangtze Block (modified after Yu et al., 2014; Li, 2018); (C) Geological sketch map of the Western Hunan Pb-Zn metallogenic belt in South China (modified after Yang and Lao, 2007), showing the distribution of Pb-Zn deposits, structures and strata.

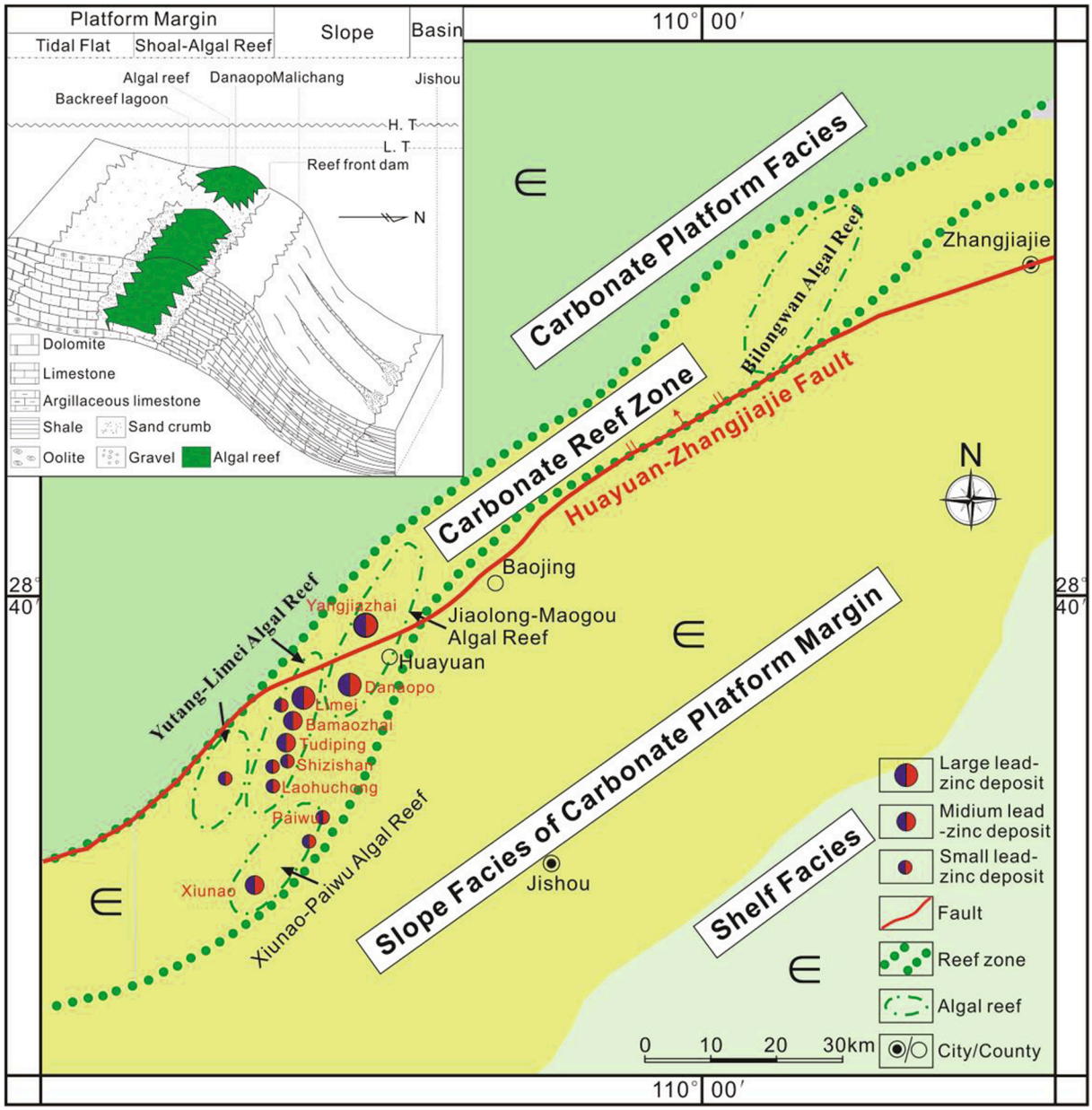

Fig. 2. Sketch map of algal reef facies model and paleogeographic environment in western Hunan-eastern Guizhou area (modified after Yu et al., 2014; Chen et al., 2018), showing the distributions of Pb-Zn deposits, faults and sedimentary facies.

Although substantial progress has been made in revealing the mineralization characteristics, the origin of the ore-forming materials of these Pb-Zn deposits are still not well constrained due to the lack of high-quality mineral S-Pb isotope data (Bao et al., 2017a; Peevlera et al., 2003; Yuan et al., 2018), thus limiting the understanding of Zn-Pb metallogenic mechanism and regularity in the WHEG. Some authors proposed a single sulfur source from seawater sulfates in the ore-bearing strata (e.g. Cai et al., 2014; Zhao et al., 2016; Cao et al., 2017), whereas some others suggested a mixed S source from the Lower Cambrian Niutitang Fm. (LCNF) and LCQF strata (e.g. Hu et al., 2017; Wei et al., 2020). The metal source(s) is also disputed among a single mantle-derived source (Shu, 1983; Li, 1992), carbonate ore host (e.g., Cai et al., 2014; Kuang et al., 2015; Li, 2018), or mixing between the Proterozoic Banxi Group (Gp.) metamorphic rocks and the underlying Cambrian ore-bearing strata (Schneider et al., 2002; Cao et al., 2017; Wei et al., 2020). Meanwhile, the metallogeny was variably attributed to sedimentary-type (Luo et al., 2009; Chen et al., 2011), sedimentary-reworking type (Li, 1992), or Mississippi Valley Type (MVT) (Yang and Lao, 2007; Cai et al., 2014; Li, 2018; Wei et al., 2020).

The newly discovered Danaopo Zn-Pb deposit (reserve: ~4.57 Mt Zn + Pb, 65279 t Cd, 758 t Ag; Yu et al., 2014), hosted by the LCQF reef limestone and controlled by the Huayuan-Zhangjiajie deep fault, is located in the middle WHEG metallogenic belt (Fig. 1A, C; Yang and Lao, 2007). The deposit shares similar geological characteristics with other Pb-Zn deposits in the belt, and is thus representative for studying the WHEG ore-forming material source and mechanism. In recent years, micro-analyses (notably LA-MC-ICP-MS and Nano SIMS technique) on mineral isotopes have been increasingly adopted to clarify the ore-

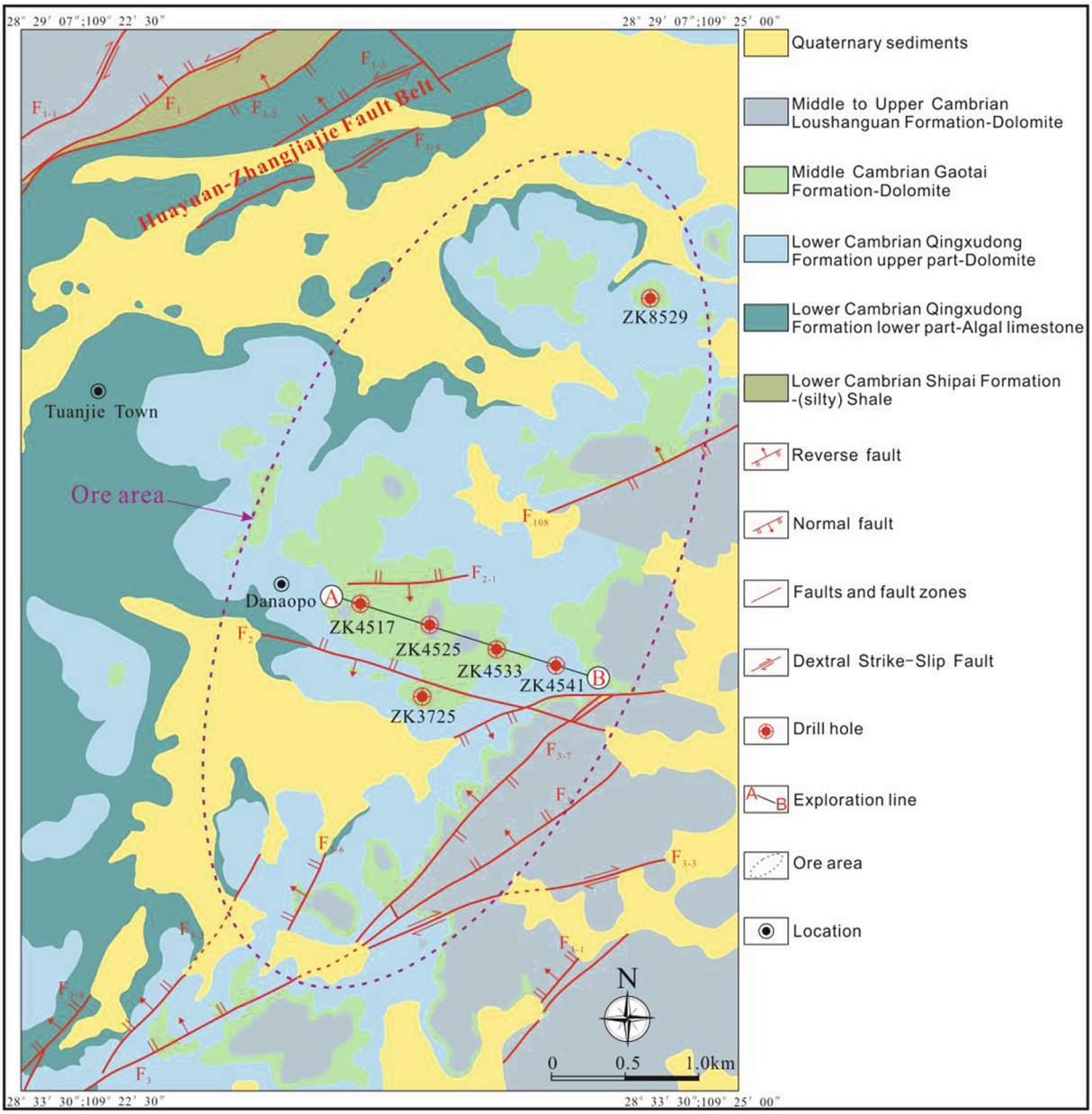

Fig. 3. Geological sketch map of the Danaopo Zn-Pb deposit (modified after Yu et al., 2014), showing the strata, faults and the drill-hole locations.

forming material and fluid source(s) (Bao et al., 2017a; Bendall et al., 2006; Chen et al., 2017; Ikehata et al., 2008; Souders and Sylvester, 2010; Yuan et al., 2018). Compared with conventional bulk-mineral S and Pb isotope analyses, the *in-situ* analytical techniques can avoid the mixing effects of the complex mineral generations or impurities, and constrain accurately the origin of ore-forming components and genesis of the deposit (Luo et al., 2019, 2020; Tan et al., 2017; Yuan et al., 2015; Zhou et al., 2018b). In this paper, therefore, detailed scanning electron microscopy (SEM) works and *in-situ* LA-MC-ICP-MS S-Pb isotope analyses of sulfates and sulfides were conducted to determine the sulfur and metal source(s) at the Danaopo deposit and constrain its ore formation. The outcomes will provide further constraints on the ore-forming mechanism of carbonate-hosted Pb-Zn deposits in the WHEG.

2. Regional geology

The Yangtze Block is bounded by the Sanjiang, Qinling, Songpan-Ganzê, and Cathaysia terranes to the west, north, northwest, and southeast, respectively (Fig. 1A, B). The Upper Yangtze comprises a crystalline basement made of the Banxi Gp. metamorphosed sandstone–siltstone and silty slate, which is overlain by Sinian to Quaternary clastic and carbonate rocks with the exceptions of Carboniferous, Jurassic, and Tertiary sequences (Li, 2018). Regional magmatism was minor and mineralization-unrelated (Yang and Lao, 2007; Duan et al., 2014). Folds and faults are widely developed by the Wuling, Xuefeng-Caledonian, Hercynian and Indosinian-Yanshanian orogenic events (Yang and Lao, 2007; Li, 2018), and anticlines/synclines and NE-striking faults control the mineralization distribution along the WHEG

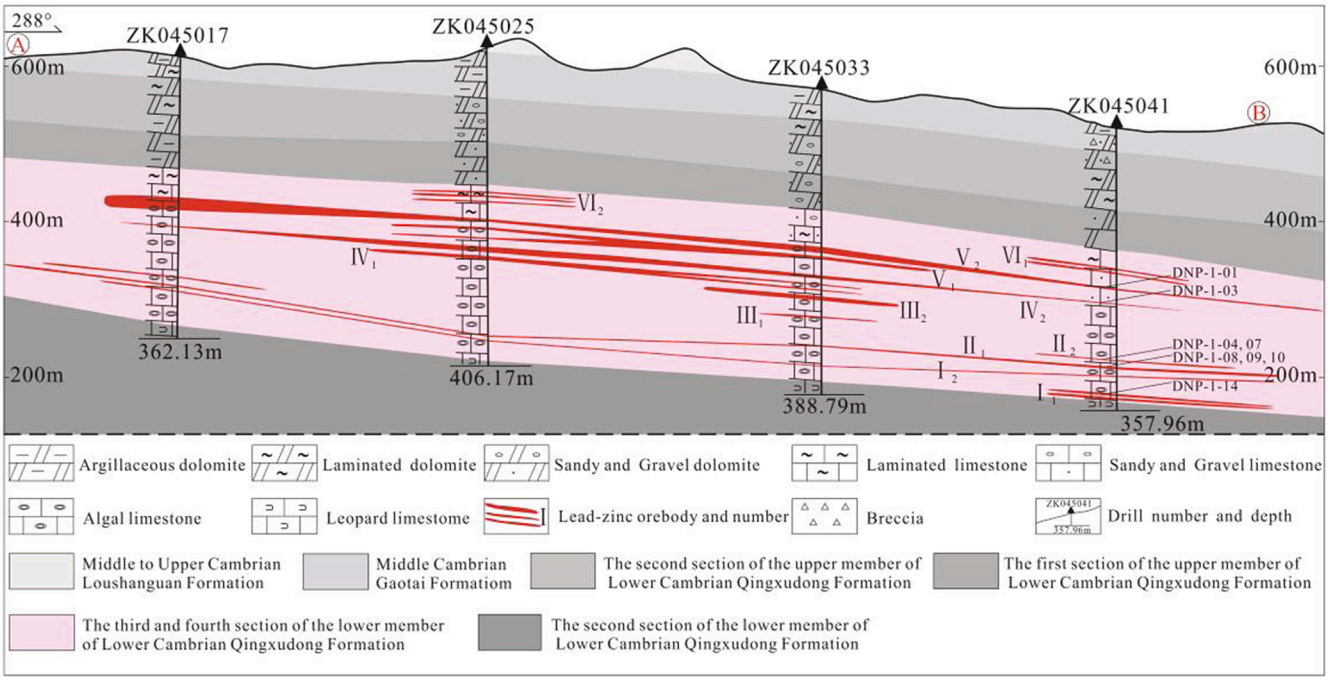

Fig. 4. Geological cross-section of the Danaopo exploration line No. 45 (modified after Yu et al., 2014), showing the distributions of orebodies and lithologic units.

metallogenic belt (Fig. 1C; Zhao et al., 2016).

In the WHEG metallogenic belt, the 300 Pb-Zn deposits discovered are hosted in the Ediacaran, Cambrian and Ordovician strata, particular in the LCQF reef limestone (Tang et al., 2012; Li et al., 2013) that controlled the distribution of the Xiunao, Bukouchang, Shizishan, Laohuchong, Limei, Bamaozhai, Danaopo, and Yangjiazhai deposits (Figs. 1C and 2; Luo et al., 2009; Yang et al., 2015; Zhou et al., 2017; Chen et al., 2018; Li, 2018). Geochronological studies of the WHEG Pb-Zn deposits remain primitive, with only a calcite Sm-Nd isotope age (422 ± 48 Ma) and a sphalerite Rb–Sr isotope age (483 ± 9 Ma) reported from the Bukouchang deposit (eastern Guizhou) (Yang et al., 2015), and a couple of other sphalerite Rb-Sr isotope ages from Rouxianshan (412 ± 6 Ma), Shizishan (410 ± 12 Ma), and Dagoudong (490 ± 6.5 Ma) (Du et al., 2012; Duan et al., 2014; Tan et al., 2018). With these ages, the WHEG Pb-Zn mineralization likely occurred in two phases during the Ordovician (~490 Ma) and Silurian (~410 Ma).

3. Deposit geology

3.1. Stratigraphy

At the Danaopo deposit, the exposed strata trend mainly north-east and are of Lower to Middle Cambrian age (Fig. 3), and comprises the Shipai, Qingxudong, Gaotai and Loushanguan Fm.. The Shipai Fm. is composed of silty and calcareous shale (Fig. 3). The Qingxudong Fm. comprises a lower member that contains four beds, i.e., (from bottom to top) (1) thin-bedded argillaceous/dolomitic limestone (Fig. 4); (2) thick-bedded leopard limestone with minor algal limestone (Fig. 4); (3) thick-bedded algal limestone (main ore host) (Fig. 4); (4) thick-bedded sandy/pebbly/oolitic/algal limestone (minor ore host) (Fig. 4). The upper member comprises a lower bed of medium-thin-bedded dolomite and medium-thick-bedded argillaceous dolomite, and an upper bed of thick-bedded dolomite and laminated micritic dolomite (Fig. 4). The Gaotai Fm. includes thick-bedded to thin argillaceous dolomite (Fig. 4). The Loushanguan Fm. is composed of (from bottom to top) thick-bedded dolomite, laminated argillaceous dolomite, and thick-bedded pebbly dolomite (Fig. 4).

3.2. Structures

Faults are well developed and control the distribution of Pb-Zn deposits in the Huayuan orefield (Fig. 1C). At the Danaopo deposit, faults are NE-, NW- and ENE-trending (Fig. 3; Mao, 2016). The NE-trending faults (F_1-group; possible ore-fluid conduits) may have formed by the syn-ore Huayuan-Zhangjiajie regional fault movement (dip angle 60°–75°) (Figs. 1–3; Wei et al., 2020). Both the NW-trending reverse faults (F_2-group; dipping 70°–81°) and ENE-trending normal faults (F_3-group; dipping 45°–70°) crosscut the Danaopo Zn-Pb orebodies (Fig. 3; Chen et al., 2018). Open-space structures developed in the carbonate rocks, including joints, stylolites and pores, serve as sites of ore deposition at the Danaopo deposit (Fu, 2011).

3.3. Orebodies

The Danaopo Zn-Pb mineralization trends northeast, covering an area of about 20 km^2 (~8 km long and ~2.4 km wide). Currently, 25 orebodies have been identified (Fig. 4; Mao, 2016), containing ~150 Mt ore at 3.06% Zn + Pb (Yu et al., 2014). The orebodies dip to the southeast (dip angle: 3°–10°), with their thickness thins out horizontally toward the margin. The footwall sequence is leopard limestone of the 2nd bed of the LCQF lower member, and the handing-wall sequence is the laminated argillaceous dolomite of the 1st bed of the LCQF upper member.

3.4. Alteration and mineralization paragenesis

The Danaopo Zn-Pb deposit contains both oxide and sulfide ores. Metallic minerals include mainly sphalerite, galena, smithsonite, cerussite, willemite, and pyrite. Non-metallic minerals include mainly calcite, dolomite, barite and fluorite (Figs. 5A–L, 6A–L, 7A–I). Ore textures include mainly vein (Fig. 5A, C, G, I, J) and disseminated (Fig. 5B, F, L), and the ore minerals are subhedral to anhedral granular (Fig. 6A–P), or have metasomatic (Fig. 6A, C, D, N, O), poikilitic (Fig. 6B, M, F, K), cataclastic (Figs. 6C and 8I), or interstitial (Fig. 6 C, G, I) texture.

The Danaopo alteration/mineralization includes diagenetic,

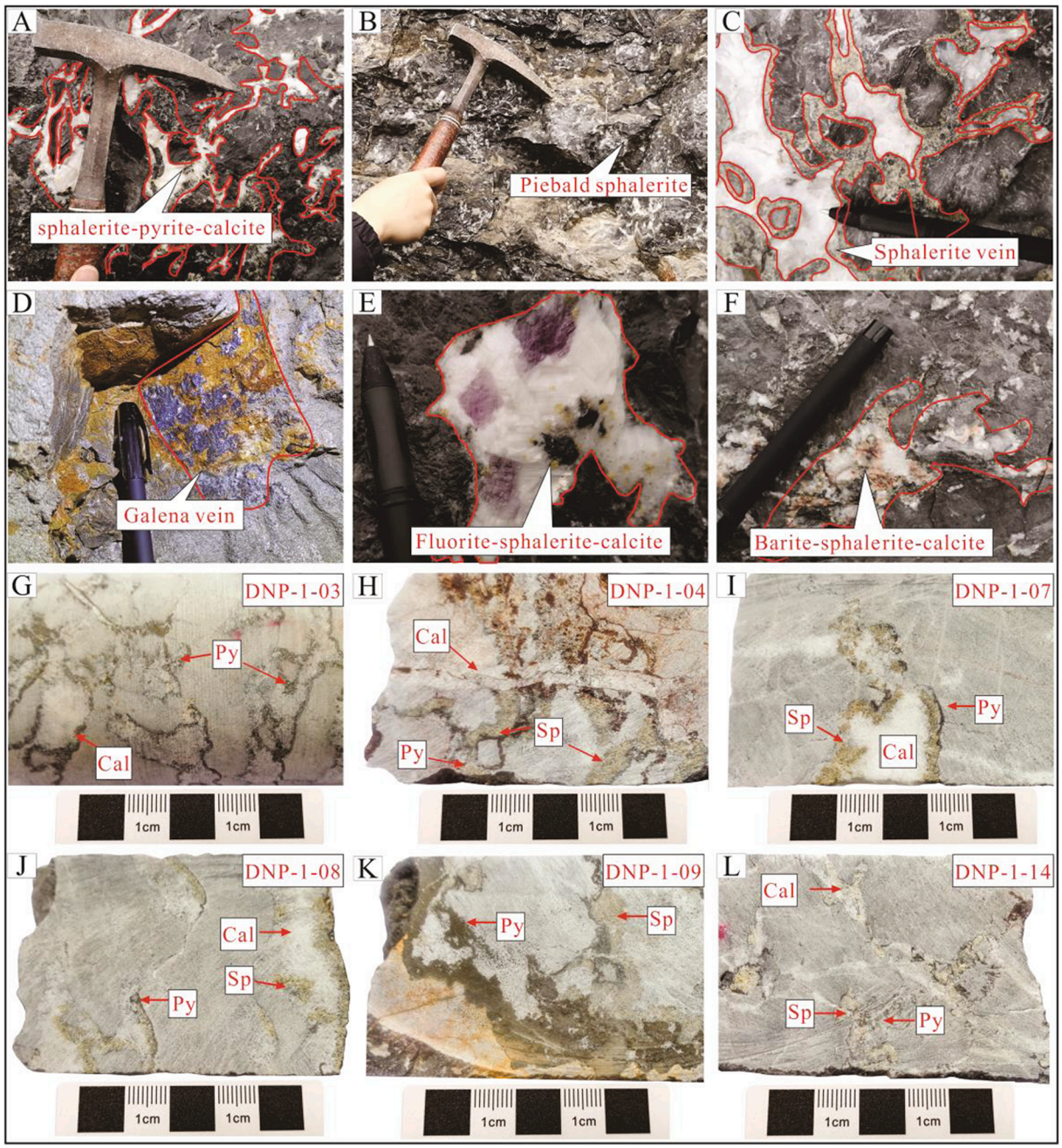

Fig. 5. Field and hand-specimen photos in the Danaopo Zn-Pb deposit; A: veined sphalerite, pyrite and calcite in algal limestone; B: sphalerite in algal limestone and the calcite with nodular and zebra (stripes) texture; C: sphalerite vein in algal limestone; D: galena vein in algal limestone; E: sphalerite and fluorite inclusions in calcite; F: sphalerite and barite in algal limestone; G: veined pyrite in algal limestone; H-K: irregular sphalerite and pyrite vein-infill in algal limestone; I-J: sphalerite and pyrite vein in algal limestone; L: sphalerite in calcite. Abbreviations: Py-pyrite; Sp-sphalerite; Gn-galena; Cal-calcite.

hydrothermal and supergene periods (Fig. 7), based on the ore cross-cutting and replacement relationship identified through optical microscopy and SEM. The hydrothermal process can be further divided into three stages, i.e., (I): pyrite + sphalerite + calcite + dolomite + fluorite; (II): sphalerite + pyrite + galena + calcite + dolomite + fluorite; (III): pyrite + galena + calcite + barite. Stage-I minerals consist mainly of subhedral coarse-grained pyrite and minor anhedral sphalerite veinlets (Fig. 6A–C, F, K, M). Stage-II is the main Pb-Zn ore-stage, and contains

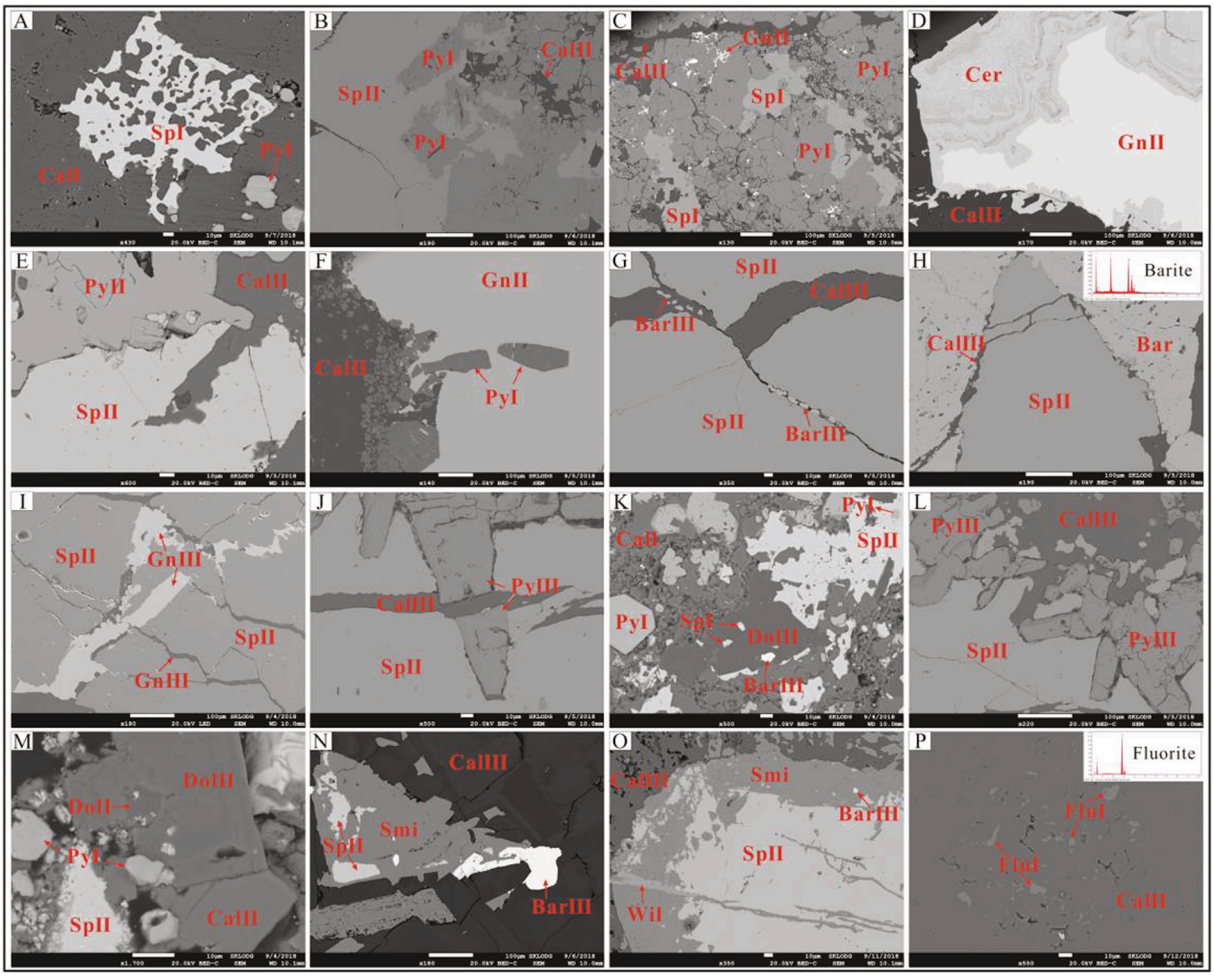

Fig. 6. Scanning electron microscope (SEM) photographs of hydrothermal minerals in different ore stages; A: anhedral Sp-I occurs as metasomatic relict in Cal-I, and Py-I has subhedral fine-grained texture; B: subhedral-anhedral Py-I filled and included by coarse-veined Sp- II; C: fine-veined Gn- II filled and replaced coarse-grained Py- II that coexists with fine-veined Sp-I. All of these are crosscut, filled and replaced by Cal- II; D: coarse-grained Gn- II in the Cal- II and oxidize to cerussite at its edge; E: subhedral granular Py- II coexists with Sp- II, both of which filled by Cal- II; F: subhedral fine-coarse granular Py-I included/replaced by coarse-grained Gn- II; G: Sp- II filled/replaced by fine-veined Cal- III and granular Bar- III; H: coarse-veined Sp- II enclosed/crosscut diagenetic barite, and both are filled/crosscut by fine-veined Cal- III; I: fine-veined Cal- III and Gn- III crosscut and fill Sp- II; J: anhedral Py- III crosscut Sp- II vein, and are both crosscut/replaced by Cal- III; K: subhedral Dol- II replaced by Bar- III includes Sp-I, and replaces and fills Sp- II which enclose fine-grained Py-I. Cal-I replaced/filled by Sp- II and Dol- II include granular euhedral-anhedral Py-I; L: subhedral Py- III fill/crosscut Sp- II, both of which are included/filled by Cal- III; M: euhedral Cal- II and Dol- II (with Dol-I inclusions) coexist with fine-veined Sp- II, all of which enclose or replace anhedral-subhedral Py-I; N: Sp- II oxidized mostly to smithsonite and replaced by anhedral Bar- III, both of which included by Cal- III; O: Sp- II partly oxidized to smithsonite and willemite, which include fine-grained Bar- III; P: anhedral Flu-I included by Cal- II. Abbreviations: Py-pyrite; Sp-sphalerite; Gn-galena; Bar-barite; Cal-calcite; Dol-dolomite; Flu-fluorite; Smi-smithsonite; Wil-willemite.

thick-veined sphalerite and subhedral coarse-grained galena, and few coarse-grained pyrite. These minerals enclose or locally replace stage-I minerals (Fig. 6D–O). Stage-III minerals include anhedral pyrite, galena and barite veinlets that crosscut or replace stage-I/-II minerals (Fig. 6I-J, N, L).

4. Sampling and analytical methods

4.1. Sampling

Sulfide ore samples were collected from three drill holes (ZK045041, ZK3725 and ZK8529) at the Danaopo deposit. Twenty-four polished thin sections were prepared and observed under the optical microscope and SEM to determine the mineral paragenesis, and ten representative samples (including barite, sphalerite, galena, and pyrite from the different ore stages) were selected for *in-situ* S-Pb isotope analyses to trace the ore-forming material source(s). The sampling location and other information were given in Fig. 3 and Table 2.

4.2. LA-MC-ICP-MS S-isotope analysis

In-situ S isotope analysis was performed at the State Key Laboratory of Continental Dynamics, Northwest University (China), using a Nu Plasma 1700 MC-ICP-MS (Nu Instruments Wrexham, UK) combined with a Resolution M-50 laser ablation system (ASI, Australia) equipped with a 193 nm ArF CompexPro102 excimer laser (Coherent, USA). For the S isotope analysis, 3.6 L/cm^2 laser energy density, 3 Hz frequency, and 25–37 μm spot size, and the single spot method were used. Helium was used as the carrier gas (flow rate: 0.28 mL/min) and Ar as the makeup gas (flow rate: 0.86 mL/min). Nu 1700 MC-ICP-MS was equipped with three ion counters and sixteen Faraday cups, of which the H5, Ax and L4 cups were used for receiving ^{34}S, ^{33}S and ^{32}S signal, respectively. In addition, sulfur compositions were calculated by relative values ($\delta^{34}S = [(^{34}S/^{32}S_{sample})/(^{34}S/^{32}S_{standard}) - 1]*1000$) with high accuracy (2SE $\leq$ 0.2‰), and the international standard IAEA-S-1 (Ag_2S, $\delta^{34}S_{VCDT} = -0.3‰$) was used. The $\delta^{34}S$ values of samples relative to IAEA-S-1 are normalized to the Vienna Cañon Diablo Troilite (VCDT). Furthermore, the standard of barite, sphalerite, pyrite and galena used

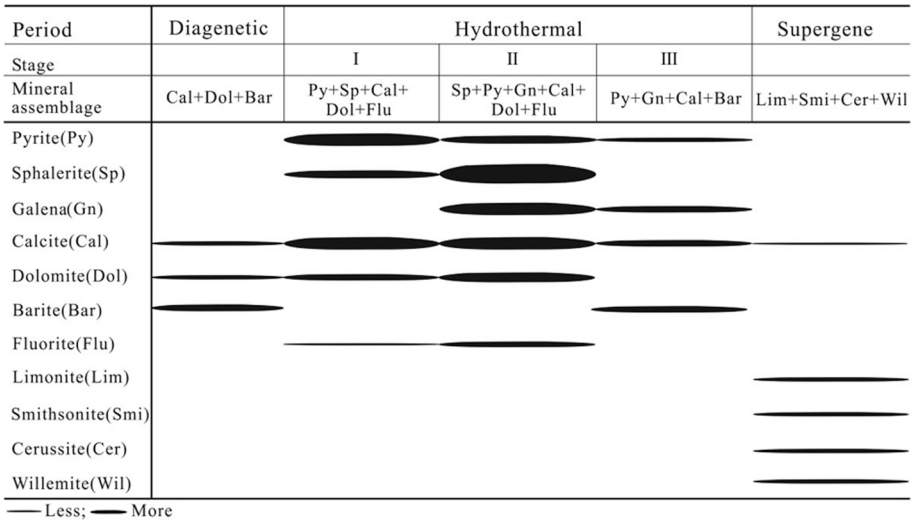

Fig. 7. Mineral paragenetic sequence in the Danaopo Zn-Pb deposit.

Table 1
The geological characteristics of orebodies in Danaopo Zn-Pb deposit (modified after Yu et al., 2014).

Orebody NO.	Occurrence(°)		Pb+Zn Reserves (tons)	Orebody Scale	Average Grade(%)		Zn/Pb Ratios	Altitude
	Dip Direction	Dip Angle			Zn	Pb		
Ⅶ	101	7	15500	small	1.84	0.65	2.8	high
$Ⅵ_2$	101	7	45795	medium	2.06	0.56	3.7	
$Ⅵ_1$	101	7	253264	large	2.24	0.97	2.3	
$Ⅴ_2$	102	7	494598	large	2.40	0.85	2.8	
$Ⅴ_1$	102	7	341238	large	1.78	0.49	3.6	
$Ⅳ_2$	102	7	375146	large	2.55	0.45	5.7	
$Ⅳ_1$	102	7	108112	large	1.91	0.24	8.0	
$Ⅲ_2$	94	7	1068090	large	3.51	0.82	4.3	
$Ⅲ_1$	94	2	160264	large	1.71	0.20	8.6	
$Ⅱ_2$	100	7	485940	large	2.73	0.22	12.4	
$Ⅱ_1$	100	7	774025	large	1.78	0.08	22.3	
$Ⅰ_2$	105	7	372022	large	1.61	0.18	8.9	
$Ⅰ_1$	105	7	75580	large	1.29	0.11	11.7	low

are NBS127 ($\delta^{34}S_{VCDT}$ = 20.3 ± 0.2‰), NBS123 ($\delta^{34}S_{VCDT}$ = 17.8 ± 0.2‰), Py-4 ($\delta^{34}S_{VCDT}$ = 1.7 ± 0.3‰) and CBI-3 ($\delta^{34}S_{VCDT}$ = 28.5 ± 0.4‰), respectively (Bao et al., 2017a; Chen et al., 2017; Yuan et al., 2018). Sample-standard bracketing (SSB) approach is used to correct instrumental drift and mass bias, during which the standards are repeatedly measured before and after each sample (standard-sample-standard). Detailed analytical methods are similar to those described in Chen et al. (2017) and Yuan et al. (2018).

4.3. LA-MC-ICP-MS Pb isotope analysis

Using the same laser ablation system as in the sulfur isotope analysis, *in-situ* Pb isotope analysis was carried out with a Nu Plasma multi-collector (MC)-ICP-MS system (Nu plasma II, Nu Instruments Wrexham, UK). In this study, the ion beam signals of ^{208}Pb, ^{207}Pb, ^{206}Pb, ^{205}Tl, ^{204}Pb + ^{204}Hg, ^{203}Tl, and ^{202}Hg were collected by the Faraday cups H2, H1, Ax, L1, L2, L3 and L4, respectively. Analytical conditions include 6 L/cm^2 laser energy density, 5 Hz frequency, 9–120 μm spot size (9 μm for galena and 100 μm for pyrite and sphalerite), helium carrier gas (flow rate: 0.28 mL/min), and the single spot method. Mass fractionation correction of Pb isotopes was calculated by exponential rule, and the fractionation factor was calculated by $^{205}Tl/^{203}Tl$ = 2.3889. The $^{204}Hg/^{202}Hg$ natural abundance ratio (0.229883) was used to determine the interference from the ^{204}Hg species on the ^{204}Pb intensity obtained, while the mass bias was corrected with the standard-sample bracketing method. The laboratory internal galena (Gn-01) standard and pressed pyrite powder tablet (PSPT-2) were used to monitor the analysis. The repeated analyses of PSPT-2 yielded reliable and reproducible results of average $^{206}Pb/^{204}Pb$ = 17.964 ± 0.003, $^{207}Pb/^{204}Pb$ = 15.620 ± 0.003, and $^{208}Pb/^{204}Pb$ = 38.167 ± 0.007 (1 s, n = 37). Detailed analytical procedures and parameter values are as described in Bao et al. (2017a) and Yuan et al. (2018).

5. Analytical results

5.1. In-situ S isotope compositions

In-situ $\delta^{34}S_{VCDT}$ values of the barite, pyrite, sphalerite, and galena

Table 2
In situ S isotopic compositions of metal sulfides formed at stage-I, -II and -III in the Danaopo deposit.

Sample NO.	Mineral	$\delta^{34}S_{VCDT}$/‰	2SE	Orebody NO.	Altitude/m	Drilling NO.
DNP-1-08	Barite	+36.5	0.2	II_1	214	ZK4541
DNP-1-08	Barite	+36.9	0.2	II_1	214	
DNP-1-09	Pyrite-I	+33.9	0.1	II_1	213	
DNP-1-09	Pyrite-I	+34.4	0.1	II_1	213	
DNP-1-09	Pyrite-I	+34.9	0.1	II_1	213	
DNP-1-09	Pyrite-I	+34.6	0.1	II_1	213	
DNP-1-09	Pyrite-I	+35.1	0.1	II_1	213	
DNP-1-10	Pyrite-I	+35.5	0.2	II_1	212	
DNP-1-10	Pyrite-I	+35.1	0.2	II_1	212	
DNP-1-14	Sphalerite-I	+35.1	0.1	I_1	180	
DNP-1-14	Sphalerite-I	+35.0	0.1	I_1	180	
DNP-1-14	Sphalerite-I	+34.9	0.1	I_1	180	
DNP-1-10	Sphalerite-I	+34.8	0.1	II_1	212	
DNP-1-09	Sphalerite-I	+34.1	0.1	II_1	213	
DNP-1-09	Sphalerite-I	+34.2	0.1	II_1	213	
DNP-1-09	Sphalerite-I	+34.5	0.1	II_1	213	
DNP-1-09	Sphalerite-I	+35.2	0.1	II_1	213	
DNP-1-08	Sphalerite-I	+34.7	0.1	II_1	214	
DNP-1-08	Sphalerite-I	+32.7	0.1	II_1	214	
DNP-1-07	Sphalerite-I	+34.0	0.2	II_2	220	
DNP-1-04	Sphalerite-I	+34.2	0.2	II_2	222	
DNP-1-03	Sphalerite-I	+33.2	0.2	IV_2	294	
DNP-1-03	Sphalerite-I	+33.3	0.2	IV_2	294	
DNP-1-03	Sphalerite-I	+33.5	0.3	IV_2	294	
DNP-1-04	Pyrite- II	+33.6	0.2	II_2	222	
DNP-1-04	Pyrite- II	+33.2	0.1	II_2	222	
DNP-1-03	Pyrite- II	+33.0	0.1	IV_2	294	
DNP-1-03	Pyrite- II	+32.9	0.1	IV_2	294	
DNP-1-03	Pyrite- II	+32.5	0.1	IV_2	294	
DNP-1-10	Sphalerite- II	+33.5	0.1	II_1	212	
DNP-1-10	Sphalerite- II	+32.3	0.1	II_1	212	
DNP-1-09	Sphalerite- II	+32.7	0.1	II_1	213	
DNP-1-08	Sphalerite- II	+32.8	0.1	II_1	214	
DNP-1-08	Sphalerite- II	+32.7	0.1	II_1	214	
DNP-1-08	Sphalerite- II	+32.6	0.2	II_1	214	
DNP-1-07	Sphalerite- II	+33.6	0.1	II_2	220	
DNP-1-07	Sphalerite- II	+33.6	0.1	II_2	220	
DNP-1-04	Sphalerite- II	+32.4	0.1	II_2	222	
DNP-1-04	Sphalerite- II	+31.9	0.2	II_2	222	
DNP-1-03	Galena- II	+28.6	0.1	IV_2	294	
DNP-1-03	Galena- II	+30.1	0.2	IV_2	294	
DNP-1-03	Galena- II	+29.2	0.2	IV_2	294	
DNP-1-03	Galena- II	+28.7	0.1	IV_2	294	
DNP-1-01	Galena-II	+29.9	0.1	V_2	326	
DNP-1-01	Galena-II	+30.0	0.1	V_2	326	
DNP-1-01	Galena-II	+29.4	0.1	V_2	326	
DNP-1-01	Galena-II	+30.1	0.1	V_2	326	
DNP-1-14	Pyrite-III	+31.6	0.2	I_1	180	
DNP-1-14	Pyrite-III	+32.3	0.2	I_1	180	
DNP-1-08	Pyrite-III	+33.0	0.1	II_1	214	
DNP-1-08	Pyrite-III	+32.0	0.1	II_1	214	
DNP-1-08	Pyrite-III	+32.7	0.1	II_1	214	
DNP-1-08	Pyrite-III	+32.6	0.1	II_1	214	
DNP-1-07	Pyrite-III	+32.4	0.1	II_2	220	
DNP-1-07	Pyrite-III	+32.0	0.1	II_2	220	
DNP-1-07	Pyrite-III	+31.1	0.1	II_2	220	
DNP-1-04	Galena-III	+25.3	0.6	II_2	222	
DNP-1-04	Galena-III	+23.9	0.2	II_2	222	
DNP-1-04	Galena-III	+23.5	0.2	II_2	222	
DNP-2-02	Sphalerite-I	+35.4	0.1	V_1	416	ZK3725
DNP-2-02	Pyrite-II	+33.6	0.2	V_1	416	
DNP-2-02	Pyrite-II	+33.7	0.2	V_1	416	
DNP-2-02	Galena-II	+29.5	0.1	V_1	416	
DNP-2-02	Galena-II	+29.6	0.2	V_1	416	
DNP-2-02	Galena-II	+29.7	0.2	V_1	416	
DNP-2-03	Barite-III	+27.1	0.2	V_1	416	
DNP-2-04	Barite-III	+28.1	0.2	V_1	416	
DNP-3-09	Galena-II	+31.0	0.2	II_2	226	ZK8529
DNP-3-09	Galena-II	+26.2	0.2	II_2	226	
DNP-3-09	Galena-II	+30.0	0.1	II_2	226	
DNP-3-09	Pyrite-III	+32.2	0.2	II_2	226	
DNP-3-09	Pyrite-III	+31.5	0.1	II_2	226	

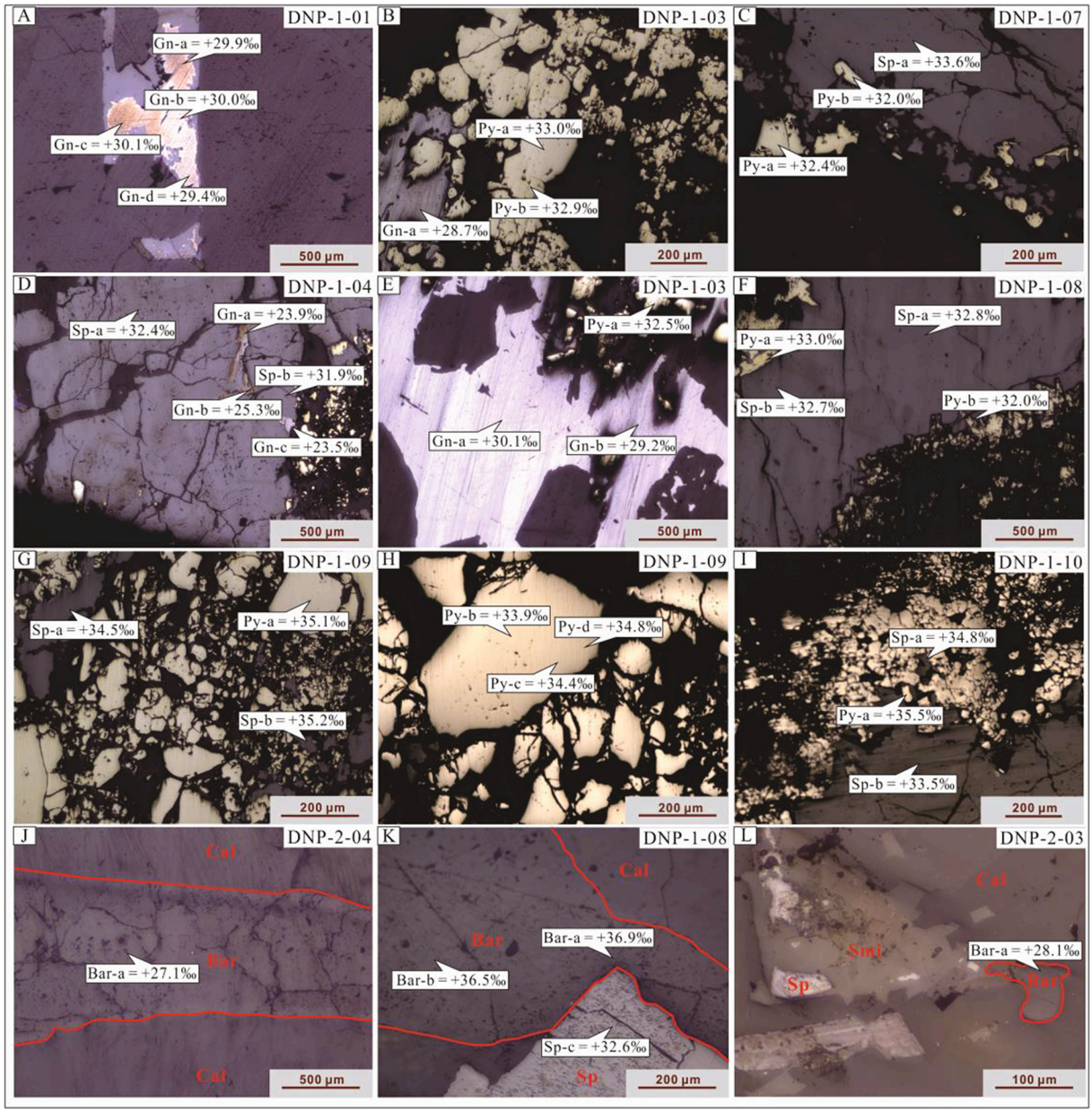

Fig. 8. Sketch for Location and S-isotope values of pyrite, sphalerite and galena from the Danaopo deposit. Abbreviations: Py-pyrite; Sp-sphalerite; Gn-galena; Bar-barite; Cal-calcite; Smi-smithsonite.

samples from the Danaopo deposit are listed in Table 2 and illustrated in Figs. 8–10. The $\delta^{34}S_{VCDT}$ values of barite in the diagenetic (Fig. 6H; Fig. 8K) and late hydrothermal stage (-III) (Fig. 6G, N, O; Fig. 8J, L) range from 36.5 to 36.9‰ (mean + 36.7‰, n = 2) and 27.1 to 28.1‰ (mean + 27.6‰, n = 2), respectively (Table 2 and 5). The hydrothermal sulfide $\delta^{34}S_{VCDT}$ values vary from +23.5 to +35.5‰ (mean + 32.2‰, n = 68), of which pyrite (+31.3 to +35.5‰, mean + 33.1‰, n = 24), sphalerite (+31.9 to +35.4‰, mean + 33.8‰, n = 26), and galena (+23.5 to +31.0‰, mean + 28.4‰, n = 17). Pyrite-I and sphalerite-I have $\delta^{34}S_{VCDT}$ values of +33.9 to +35.5‰ (mean + 34.8‰, n = 17) and +32.7 to +35.4‰ (mean + 34.3‰, n = 16), respectively, whilst those for pyrite-II, sphalerite-II, and galena-II are +32.5 to +33.7‰ (mean + 33.2‰, n = 7), +31.9 to + 33.6‰ (mean + 32.8‰, n = 9), and +26.2 to +31.0‰ (mean + 29.3‰, n = 14), respectively. Pyrite-III and galena-III have $\delta^{34}S_{VCDT}$ values of +31.1 to +33.0‰ (mean + 32.1‰, n = 11) and +23.5 to +25.3‰ (mean + 24.2‰, n = 3), respectively. In addition, *in-situ* sulfide $\delta^{34}S$ values follow the decreasing order of $\delta^{34}S_{Py\text{-}I} > \delta^{34}S_{Sp\text{-}I}$, $\delta^{34}S_{Py\text{-}}$ II > $\delta^{34}S_{Sp\text{-}}$ II > $\delta^{34}S_{Gn\text{-}}$ II and $\delta^{34}S_{Py\text{-}}$ III > $\delta^{34}S_{Gn\text{-}}$ III.

5.2. *In-situ* Pb isotope compositions

In-situ Pb isotope compositions of the pyrite, sphalerite and galena samples are listed in Table 3 and plotted in Figs. 11 and 12. The sample data (n = 36) are summarized as follows: $^{206}Pb/^{204}Pb$ = 18.144–18.254 (mean 18.200), $^{207}Pb/^{204}Pb$ = 15.718–15.797 (mean 15.751) and $^{208}Pb/^{204}Pb$ = 38.378–38.605 (mean 38.485), with $^{238}U/^{204}Pb$ (μ) values of 9.7–9.9 (mean 9.8). Moreover, sulfides of different altitudes (180–416 m) or ore stages (−I/−II/−III) have similar Pb isotope compositions (Figs. 11 and 12). $^{206}Pb/^{204}Pb$, $^{207}Pb/^{204}Pb$ and $^{208}Pb/^{204}Pb$ ratios of the sphalerite samples (n = 10) are of 18.189–18.254 (mean 18.219), 15.734–15.797 (mean 15.765), and 38.439–38.591 (mean 38.518), respectively, whilst those of the pyrite (n = 10) are of 18.154–18.238 (mean 18.201), 15.726–15.780 (mean 15.747) and 38.406–38.605 (mean 38.484), respectively. The galena samples (n =

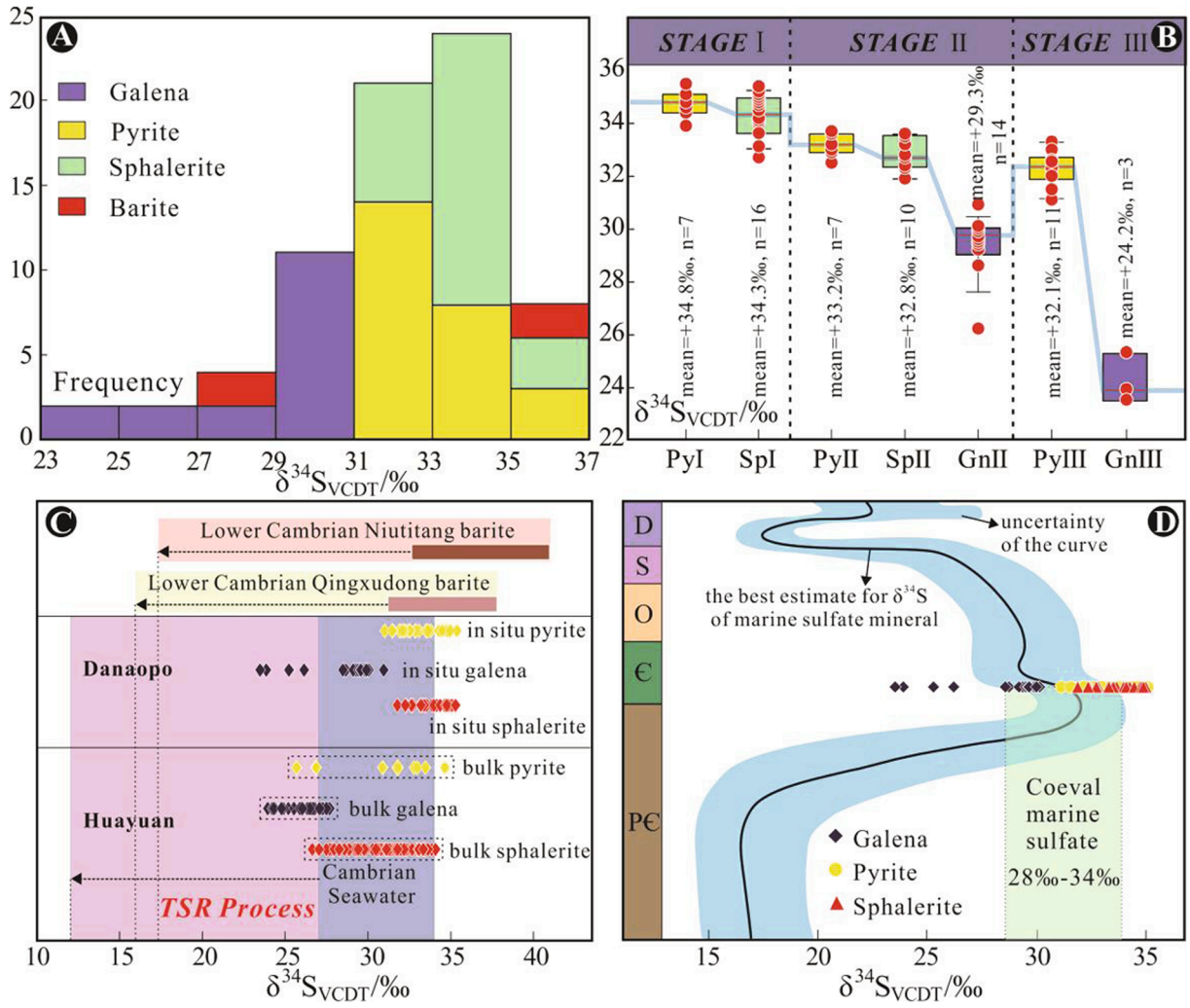

Fig. 9. (A) S-isotope histogram for the Danaopo deposit; (B) Box plot of S isotope compositions of sulfides from different ore stages; (C) Comparison of sulfide $\delta^{34}S$ values between the Danaopo deposit and the rest of the Huayuan orefield (Cai et al., 2014; Duan et al., 2014; Zhou et al., 2016; Cao et al., 2017; Wei, 2017). Cambrian seawater (Claypool et al., 1980), Qingxudong Fm. barite (Liu and Lu, 2000; Duan et al., 2014; Zhou et al., 2016; Wei et al., 2017), and Niutitang Fm. (Fan et al., 1986) data are also shown for comparison; (D) Comparison between S isotope compositions of Danaopo deposit and coeval marine evaporites (modified after Claypool et al., 1980).

16) have $^{206}Pb/^{204}Pb$ = 18.144–18.211 (mean 18.187), $^{207}Pb/^{204}Pb$ = 15.718–15.746 (mean 15.743), and $^{208}Pb/^{204}Pb$ = 38.378–38.512 (mean 38.463) (Table 3).

6. Discussion

6.1. Source(s) of sulfur and sulfate reduction mechanism

The $\delta^{34}S_{VCDT}$ compositions and fractionation of S-bearing minerals have been used to trace ore-forming material source and constrain the ore-forming mechanism (Ohmoto, 1972; Rye and Ohmoto, 1974; Jones and Kesler, 1997; Seal et al., 2000; Yuan et al., 2018). However, due to the great influence of physical–chemical conditions including fo_2, pH, ionic strength and temperature in the ore-forming fluid, $\delta^{34}S_{sulfides}$ are always not equivalent to $\delta^{34}S_{\Sigma S}$ (Ohmoto, 1972; Chu et al., 1984; Seal, 2006). If significant amounts of sulfates were formed in the main-ore stage, then $\delta^{34}S_{sulfate} > \delta^{34}S_{\Sigma S} > \delta^{34}S_{sulfides}$, otherwise $\delta^{34}S_{sulfides} \approx \delta^{34}S_{\Sigma S}$ (Ohmoto, 1972).

Sulfur-bearing minerals at the Danaopo deposit consist of barite, sphalerite, galena, and pyrite. *In-situ* $\delta^{34}S_{VCDT}$ values of metal sulfides range from +23.5 to +35.5‰ (mean + 32.2‰, n = 68) (Tables 2 and 5) and barite formed at diagenetic and late-hydrothermal stage are 36.5–36.9‰ and 27.1–28.1‰ (Figs. 6–8; Tables 2 and 5), respectively. The minor amount of hydrothermal barite-III (Fig. 6G, O, N; Fig. 8J, L) after the main Zn-Pb mineralization stage would make little influence on the sulfur isotope compositions of the hydrothermal fluid system (Ohmoto, 1972). Thus, the Danaopo ore-fluid $\delta^{34}S_{\Sigma S}$ values approximate the mean $\delta^{34}S_{pyrite}$ values of +33.1‰ (+31.3 to +35.5‰, n = 24). In addition, the sulfide $\delta^{34}S$ values gradually decrease in the trend of $\delta^{34}S_{Py} > \delta^{34}S_{Sp} > \delta^{34}S_{Gn}$ (Fig. 9B; Table 2), which indicates that the ore-forming fluids were enriched in heavy S isotopes, consistent with what would be expected in thermodynamic equilibrium fractionation.

In many medium–low temperature hydrothermal deposits, sulfates (SO_4^{2-}) in the seawater or sediments can be reduced to sulfide (S^{2-}) via bacterial sulfate reduction (BSR) or thermochemical sulfate reduction (TSR) (Ohmoto and Rye, 1979; Machel et al., 1995; Leach et al., 2005), depending on the temperature (Machel et al., 1995). BSR usually takes place at 60–80 °C (Machel, 1989), although its occurrence at 110 °C has also been reported (Jørgenson et al., 1992). BSR commonly produces a wide $\delta^{34}S_{VCDT}$ range due to the large isotopic fractionation (15–66‰) between sulfate and sulfide (Rees, 1973; Leach et al., 2005; Basuki et al., 2008; Sim et al., 2011; Li et al., 2019). In contrast, TSR (occur at 100–140 °C) produces relatively narrow range for sulfur isotopic fractionation, yielding <15‰ in the presence of organic matter (Ohmoto

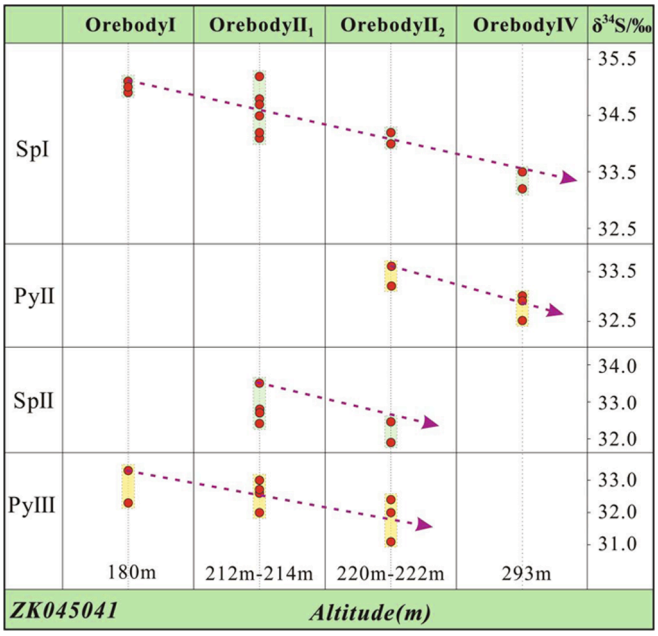

Fig. 10. Plot of $\delta^{34}S$ of sulfides at different ore stages vs. altitudes of orebodies from the Danaopo deposit.

and Rye, 1979; Worden et al., 1995; Wang et al., 2018). Previous studies indicate that the fluid inclusions (from the Danaopo calcite and sphalerite) homogenized mainly at 140–328 °C (Zhou et al., 2015). We obtained similar sulfur equilibrium temperature (147–300 °C) for coexisting sulfides (pyrite-galena and pyrite-sphalerite) (Table 4), based on the sulfur isotope balance fractionation equation (Rye et al., 1974). Hence, we suggested that TSR was more likely for the case of the Danaopo deposit, as also supported by the small narrow sulfide $\delta^{34}S_{VCDT}$ range (+30 to +35‰) (Fig. 9A). In addition, the sulfide $\delta^{34}S_{VCDT}$ values of the same ore stage decrease with the increase of altitude (Fig. 10), suggesting that hydrothermal fluid temperature decreased during the fluid ascend, which weakened the TSR process.

Although $\delta^{34}S_{VCDT}$ values of the Danaopo sulfides (+23.5 to +35.5‰, mean + 32.2‰) are slightly higher and with wider-range than those of bulk $\delta^{34}S_{VCDT}$ values of single-type sulfide minerals from eight representative Pb-Zn deposits in the Huayuan orefield (+24.0 to +34.1‰, mean + 29.4‰, n = 149; Fig. 9C and Table 5), the small difference indicates that the whole Huayuan orefield has had similar sulfur source (Fig. 9C). In Fig. 9A, it is shown that the sulfur source of the Danaopo ore-forming fluid is single-sourced. Besides, the sulfide $\delta^{34}S_{VCDT}$ values have no significant intra-grain variation (e.g., from core to rim) (Fig. 8A, B, E, F, H), which further supports a single sulfur source. It is clear that sulfur isotope compositions of the Danaopo sulfides are different from typical mantle rocks (−4 to +8‰; Chaussidon et al., 1989), metamorphic rocks (−20 to +20‰; Chen and Wang, 2004), or igneous rocks (−5 to +10‰; Seal et al., 2000), but similar to the Cambrian seawater sulfate (+28 to +34‰; Fig. 9D; Claypool et al., 1980), diagenetic barite (+32.8 to +37.3‰) from the LCQF ore host (Tables 4 and 5; Liu and Zheng, 2000; Zhou et al., 2016; Wei, 2017), and barite (+33 to +41‰) in the footwall LCNF sequence (Fig. 9C; Table 5; Fan et al., 1986). The sulfur may thus be derived from ore-bearing or footwall sequences at the Danaopo deposit. If the sulfur was sourced from the LCNF sulfates, the theoretical TSR-generated sulfide S-isotope values could range from +18 to +41‰, broadly similar to the measured $\delta^{34}S_{VCDT}$ values (+23.5 to +35.5‰). However, this contrasts with to the

Table 3
In situ Pb isotopic compositions of metal sulfides formed at stage-I, -II and -III in the Danaopo deposit.

Sample NO.	Mineral	$^{208}Pb/^{204}Pb$	1 s	$^{207}Pb/^{204}Pb$	1 s	$^{206}Pb/^{204}Pb$	1 s
DNP-1-03	Galena-II	38.497	0.007	15.752	0.003	18.199	0.002
DNP-1-03	Galena-II	38.504	0.004	15.745	0.002	18.205	0.002
DNP-1-03	Galena-II	38.512	0.004	15.746	0.002	18.211	0.002
DNP-1-01	Galena-II	38.450	0.004	15.751	0.002	18.177	0.002
DNP-1-01	Galena-II	38.438	0.005	15.745	0.002	18.171	0.002
DNP-1-01	Galena-II	38.415	0.005	15.735	0.002	18.156	0.002
DNP-2-02	Galena-II	38.453	0.003	15.738	0.001	18.191	0.001
DNP-2-02	Galena-II	38.441	0.003	15.743	0.001	18.182	0.001
DNP-2-02	Galena-II	38.447	0.004	15.742	0.001	18.182	0.002
DNP-3-09	Galena-II	38.454	0.004	15.752	0.002	18.189	0.002
DNP-3-09	Galena-II	38.414	0.005	15.728	0.002	18.168	0.002
DNP-3-09	Galena-II	38.378	0.005	15.718	0.002	18.144	0.002
DNP-1-04	Galena-III	38.497	0.005	15.747	0.002	18.201	0.002
DNP-1-04	Galena-III	38.507	0.005	15.751	0.002	18.206	0.002
DNP-1-04	Galena-III	38.497	0.005	15.749	0.002	18.204	0.002
DNP-1-04	Galena-III	38.500	0.007	15.748	0.002	18.203	0.003
DNP-1-09	Pyrite-I	38.605	0.014	15.780	0.005	18.238	0.005
DNP-1-04	Pyrite-II	38.471	0.026	15.740	0.010	18.186	0.012
DNP-1-03	Pyrite-II	38.514	0.018	15.747	0.008	18.211	0.008
DNP-1-03	Pyrite-II	38.479	0.007	15.742	0.003	18.202	0.003
DNP-1-14	Pyrite-III	38.513	0.009	15.765	0.004	18.208	0.004
DNP-1-14	Pyrite-III	38.437	0.019	15.733	0.008	18.197	0.008
DNP-1-08	Pyrite-III	38.526	0.016	15.769	0.006	18.218	0.008
DNP-1-07	Pyrite-III	38.452	0.011	15.745	0.004	18.201	0.005
DNP-1-07	Pyrite-III	38.428	0.019	15.732	0.007	18.193	0.009
DNP-3-09	Pyrite-III	38.406	0.018	15.726	0.007	18.154	0.008
DNP-1-07	Sphalerite-I	38.591	0.026	15.797	0.010	18.254	0.012
DNP-1-07	Sphalerite-I	38.547	0.017	15.777	0.007	18.233	0.008
DNP-1-07	Sphalerite-I	38.558	0.009	15.781	0.003	18.231	0.004
DNP-1-14	Sphalerite-II	38.500	0.022	15.754	0.009	18.213	0.010
DNP-1-09	Sphalerite-II	38.450	0.019	15.750	0.008	18.211	0.009
DNP-1-09	Sphalerite-II	38.516	0.015	15.758	0.006	18.220	0.007
DNP-1-08	Sphalerite-II	38.489	0.012	15.754	0.005	18.201	0.005
DNP-1-08	Sphalerite-II	38.439	0.007	15.734	0.003	18.189	0.003
DNP-1-08	Sphalerite-II	38.529	0.021	15.770	0.009	18.215	0.010
DNP-1-04	Sphalerite-II	38.514	0.017	15.758	0.007	18.206	0.008

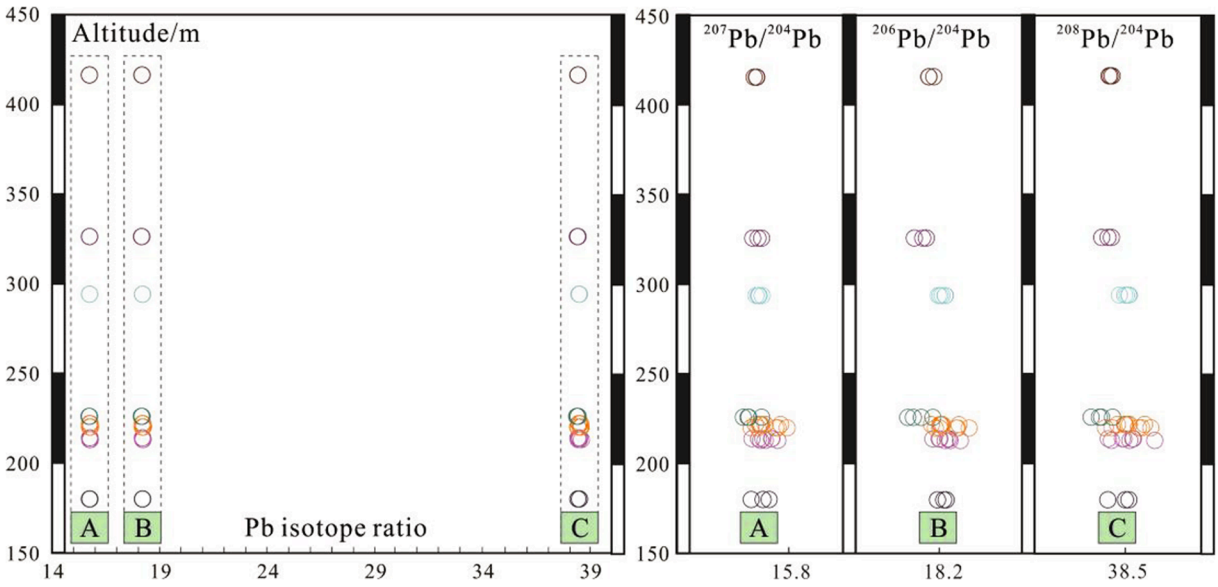

Fig. 11. Plot of $^{206}Pb/^{204}Pb$, $^{207}Pb/^{204}Pb$, and $^{208}Pb/^{204}Pb$ ratios vs. altitude of the samples (modified after Bao et al., 2017b), displaying relatively homogenous Pb isotope characteristics of the Danaopo deposit.

common interpretation that the Niutitang Fm. contributed much of the ore-forming metals for Danaopo. Because the Niutitang Fm. is rich in organic matters (You, 2010; Liu, 2017), which would have reacted with sulfate to generate reduced sulfur, which then precipitated the ore metals in the LCNF rather than in the upper LCQF through a long-distance transport.

Hence, the LCQF marine sulfates may have supplied most of the sulfur, because: (1) in the early sedimentary diagenetic stage, the decay of algae, bioclastic and other micro-organisms in the ore-bearing strata can produce abundant HS^-, H_2S and CH_4 (Liu and Lu, 2000; Tang et al., 2012, 2013; Kuang et al., 2015); (2) the bitumen and other hydrocarbons in the ore-bearing strata, as evidenced by fluid inclusion studies (Liu et al., 1999b, 1999a; Wei, 2017), may have provided the reductants for TSR in the Huayuan orefield; (3) the presence of gypsum in fluid inclusions (Liu et al., 1999a; Wei, 2017) and the calcite as nodular and zebra (stripes) texture (Fig. 5B) support that evaporates were once present (Leach, 2014), and provided the ore-forming sulfur; (4) the theoretical $\delta^{34}S_{VCDT}$ values of sulfide ranging from +17.8‰ to +37.3‰ by TSR reaction of sulfate in the LCQF match appropriately with the new-obtained $\delta^{34}S_{VCDT}$ values (+23.5‰ to +35.5‰) in the Danaopo deposit and the surface of barite contain many dissolution holes under SEM (Fig. 6H), which is a probable evidence that such barite provide sulfur for mineralization.

6.2. Metals source

The Caledonian orogeny in South China led to the formation of Xuefeng Uplift in western Hunan (Feng et al., 2003; Du and Xu, 2012). The Xuefeng Uplift may have experienced a tectonothermal event slightly before 419 Ma, and the influence reached as far west as the Huayuan-Zhangjiajie fault zone (Hu et al., 2010). In addition, sphalerite dating results (410–490 Ma) (Du et al., 2012; Duan et al., 2014; Tan et al., 2018) indicate that the Huayuan Pb-Zn mineralization occurred in the late Silurian to early Ordovician. Hence, Pb isotope ratios of the LCQF reef limestone (Schneider et al., 2002; Cai et al., 2014; Hu et al., 2017), LCNF black shale (Schneider et al., 2002; Chen et al., 2003), and the Proterozoic Banxi Gp. slate (Liu and Zhu, 1994) were corrected (Table 6) with the sphalerite Rb-Sr isochron age (410 ± 12 Ma) (Duan et al., 2014) from the Shizishan Pb-Zn deposit (Fig. 1C).

Previous Pb isotope data of 63 single sulfide minerals (pyrite, sphalerite and galena) analyzed by the solution method in the Huayuan Pb-Zn orefield have scattered compositions (Fig. 12 A, C), i.e., $^{206}Pb/^{204}Pb$ = 17.91–18.83, $^{207}Pb/^{204}Pb$ = 15.53–15.83, and $^{208}Pb/^{204}Pb$ = 37.57–39.26 (Table 6), which indicate mantle-derived (Li, 1992), mantle-crust mixing (Shu, 1983; Kuang et al., 2015; Cao et al., 2017) or crustal (Hu et al., 2017; Wei et al., 2017) source(s), respectively. By comparison, the sulfides from Danaopo have narrower Pb isotope ranges, i.e., $^{206}Pb/^{204}Pb$ = 18.14–18.24, $^{207}Pb/^{204}Pb$ = 15.72–15.80, and $^{208}Pb/^{204}Pb$ = 38.38–38.61 (Figs. 11, 12 A, C; Table 6). In the $^{207}Pb/^{204}Pb$ vs. $^{206}Pb/^{204}Pb$ plot (Fig. 12A), the Danaopo samples fall above the average upper crustal Pb evolution curve (Zartman and Doe, 1981), suggesting that the metals were mainly upper crustal-derived. All data points fall into a steeply linear trend (Fig. 12B, D), indicating that the lead may have been derived from a single Pb source or the lead isotopes were homogenized by thorough source mixing (Carr et al., 1995; Canals and Cardellach, 1997; Cunha et al., 2007; Ding et al., 2016).

There are three potential upper-crustal lead sources in the Huayuan Pb-Zn orefield, namely the ore-hosting LCQF reef limestone, the LCNF black shale, and the Proterozoic Banxi Gp. basement rocks (Schneider et al., 2002; Cao et al., 2017; Hu et al., 2017; Wei et al., 2020). Comparing the Pb isotope compositions of the Danaopo sulfides with those of the age-corrected (410 Ma) wall-rocks and basement rocks, the former is clearly different from each of the potential Pb source (Table 6), suggesting that a single Pb source can be excluded. The sulfides show very similar $^{206}Pb/^{204}Pb$ ratios with the reef limestone, black shale and slates for the same $^{206}Pb/^{204}Pb$ ratios (Fig. 12A, C), albeit minor differences do exist as follows: (1) although sulfides have similar Pb isotope composition with reef limestones, the former have slightly higher $^{207}Pb/^{204}Pb$ and $^{208}Pb/^{204}Pb$ than the latter (Fig. 12A, C; Table 6); (2) sulfides also display both higher $^{207}Pb/^{204}Pb$ and $^{208}Pb/^{204}Pb$ ratios than black shales at a given $^{206}Pb/^{204}Pb$ ratio, despite the black shales have a wider range Pb isotope ratios than that of sulfides (Fig. 12A, C; Table 6); (3) sulfides show higher $^{207}Pb/^{204}Pb$ and lower $^{208}Pb/^{204}Pb$

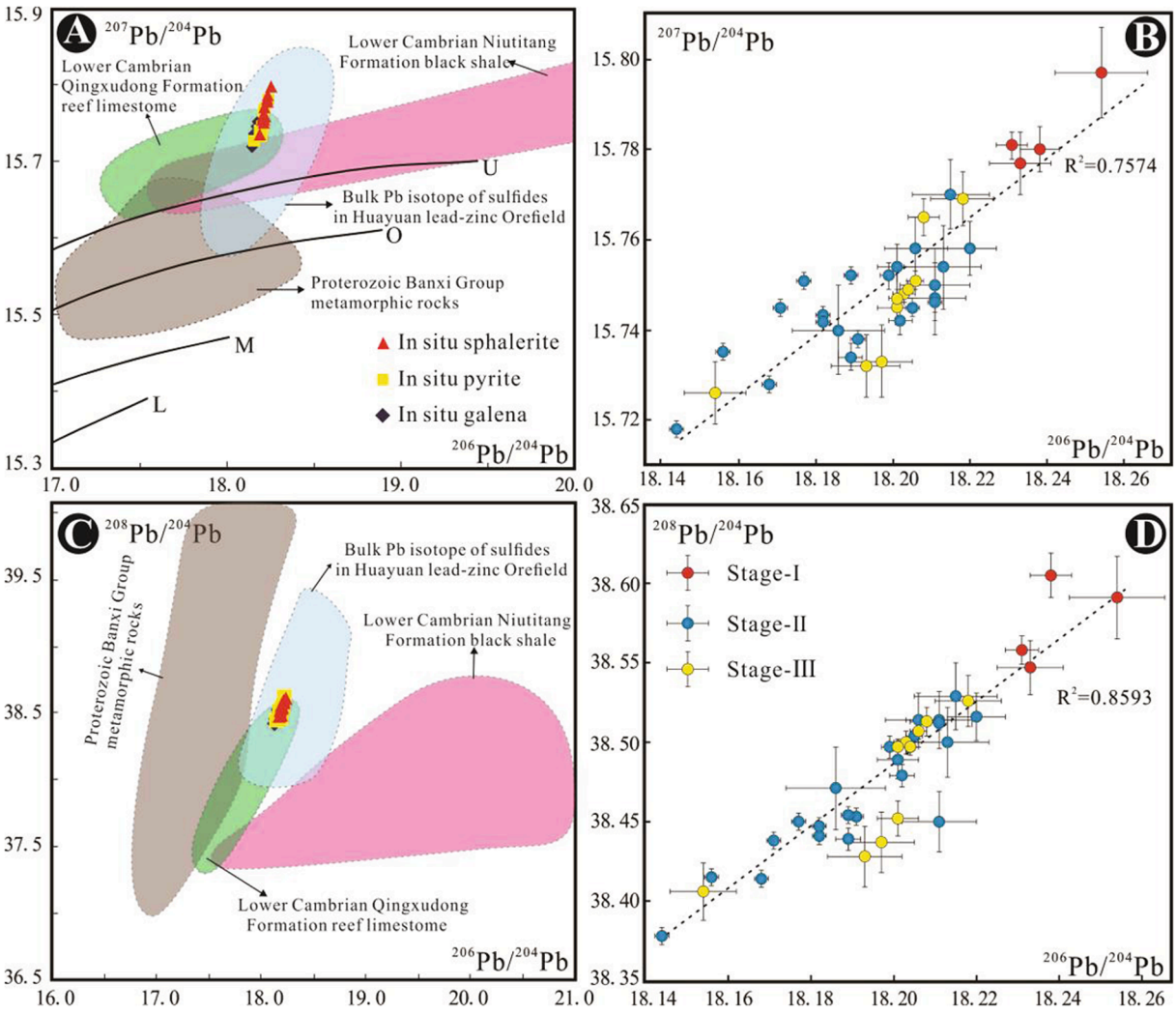

Fig. 12. (A, C) Diagrams of $^{207}Pb/^{204}Pb$ vs. $^{206}Pb/^{204}Pb$ and $^{208}Pb/^{204}Pb$ vs. $^{206}Pb/^{204}Pb$ for the Danaopo deposit. Data source: Pb isotope evolution curves of Upper Crust (U), Orogenic Belt (O), Mantle (M) and Lower Crust (L) (Zartman and Doe, 1981); Pb-Zn deposits in the Huayuan orefield (Cai et al., 2014; Zhou et al., 2016; Cao et al., 2017; Wei, 2017; Li, 2018); age-corrected (t = 410 Ma) Qingxudong Fm. reef limestone (Schneider et al., 2002; Cai et al., 2014; Hu et al., 2017), Niutitang Fm. black shale (Schneider et al., 2002; Chen et al., 2003), and Banxi Gp. slate (Liu and Zhu, 1994); (B, D) Plots of $^{207}Pb/^{204}Pb$ vs.$^{206}Pb/^{204}Pb$ and $^{208}Pb/^{204}Pb$ vs. $^{206}Pb/^{204}Pb$ for the Danaopo stage-I to -III sulfides.

Table 4
Temperature of symbiotic sulfides calculated by sulfur isotope geothermometer (Ohmoto and Rye, 1979).

Samples	$\delta^{34}S$/‰-Py	$\delta^{34}S$/‰-Sp	$\delta^{34}S$/‰-Gn	T (°C)	Period
DNP-1-03	+32.5		+28.6	215	Stage-II
DNP-1-03	+32.9		+28.7	197	Stage-II
DNP-1-03	+33.0		+29.2	222	Stage-II
DNP-2-02	+33.6		+29.5	203	Stage-II
DNP-2-02	+33.7		+29.6	203	Stage-II
DNP-2-02	+33.6		+29.7	215	Stage-II
DNP-2-02	+33.7		+29.5	195	Stage-II
DNP-1-04	+33.6	+32.4		165	Stage-II
DNP-1-04	+33.2	+31.9		147	Stage-II
DNP-1-09	+35.1	+34.1		206	Stage-I
DNP-1-09	+35.1	+34.2		232	Stage-I
DNP-1-09	+34.8	+34.1		300	Stage-I
DNP-1-10	+35.5	+34.8		300	Stage-I

$\Delta^{34}S_{Py\text{-}Gn} = \delta^{34}S_{Py} - \delta^{34}S_{Gn} = 0.93 \times 10^6/(T + 273.15)^2$; $\Delta^{34}S_{Py\text{-}Sp} = \delta^{34}S_{Py} - \delta^{34}S_{Sp} = 0.23 \times 10^6/(T + 273.15)^2$ (Rye et al., 1974). Abbreviations: Py-pyrite; Sp-sphalerite; Gn-galena

than slates at a given $^{206}Pb/^{204}Pb$ ratio (Fig. 12A, C; Table 6). The Pb isotopic evidence suggests that it is possible to provide all $^{206}Pb/^{204}Pb$ and the lower end-member of $^{207}Pb/^{204}Pb$ and $^{208}Pb/^{204}Pb$ in sulfides for no matter ore-bearing or underlying strata, whereas the higher end-member of $^{207}Pb/^{204}Pb$ and $^{208}Pb/^{204}Pb$ in sulfides should be supplied by the LCNF black shale and the Banxi Gp. basements rocks, respectively. Hence, we considered that the lead (and probably other metals) was derived from thorough mixing of lead from the limestone, black shale and basement rocks.

In fact, the age-corrected (410 Ma) sphalerite Sr isotope ratios are slightly higher than those of the ore host, but generally lower than those of the footwall and basement rocks, suggesting that the footwall may have provided more radiogenic Sr (Schneider et al., 2002; Li, 2018; Wei, 2017). Besides, the LCQF in western Hunan alone may not be able to provide enough Pb (10.1 ppm) and Zn (14.9 ppm) (Lei et al., 2013) for the world-class Huayuan Pb-Zn orefield with 10 Mt proven Zn + Pb reserve (Wei et al., 2020). Since the early-stage sulfides have more radiogenic Pb isotopes than those of the main and late ore stages (Fig. 12B, D), the lower radiogenic upper-crustal lead may have been provided by both the Qingxudong and Niutitang Fm..

Published experiment studies indicate that interactions between CO_2-rich brine and shale can extract metals (e.g., Co, Cu, Pb, Zn) from

Table 5
Sulfur isotopic compositions of metal sulfides and barites from Ore-hosting strata in Huayuan Pb-Zn orefield and barite of ore-bearing underlying strata.

Deposit/Area	Strata	Mineral/Rock	$\delta^{34}S$/‰	Mean/‰	Number	Source	Method
Danaopo Zn-Pb deposit	ϵ_1q	Sulfides	+23.5–+35.5	+32.2	67	This paper	*In situ* analysis
Danaopo Zn-Pb deposit		Barites	+27.1–+36.9	+32.2	4		
Limei Pb-Zn deposit		Sphalerite	+27.0–+32.4	+30.2	18	Li, 2018	Bulk analysis
Limei Pb-Zn deposit		Sulfides	+25.2–+31.3	+28.9	18	Cao et al., 2017	
Limei Pb-Zn deposit		Sphalerite	+28.8–+32.7	+30.3	7	Cai et al., 2014	
Limei Pb-Zn deposit		Sphalerite and Galena	+27.6–+33.4	+29.9	5	Wei, 2017	
Shizishan Pb-Zn deposit		Sulfides	+26.7–+32.9	+30.8	20	Cao et al., 2017	
Shizishan Pb-Zn deposit		Sulfides	+26.3–+34.1	+30.1	15	Cai et al., 2014	
Tudiping Pb-Zn deposit		Sphalerite and Galena	+25.2–+32.2	+30.1	10	Li, 2018	
Baomaozhai Pb-Zn deposit		Sphalerite and Galena	+33.2–+33.9	+33.6	3	Wei, 2017	
Laohuchong Pb-Zn deposit		Sphalerite and Galena	+27.2–+33.8	+30.7	5	Wei, 2017	
Naizibao Pb-Zn deposit		Sulfides	+24.0–+33.4	+28.3	18	Cao et al., 2017	
Dashigou Pb-Zn deposit		Sphalerite and Galena	+24.5–+32.7	+30.7	27	Wei, 2017	
Changdengpo Pb-Zn deposit		Sphalerite and Galena	+28.7–+33.2	+31.0	3	Wei, 2017	
Huayuan Pb-Zn orefield		Barite	+36.3	–	–	Liu and Zheng, 2000	
Baomaozhai Pb-Zn deposit		Barite	+37.3	+37.3	1	Wei, 2017	
Tudiping Pb-Zn deposit		Barite	+36.1	+36.1	1	Wei, 2017	
Limei Pb-Zn deposit		Barite	+32.8–+34.2	+33.5	6	Zhou et al., 2016	
West Hunan	ϵ_1n	Barite	+33.1–+41.0	+38.2	6	Fan et al., 1986	

Table 6
Lead isotopic compositions of sulfides in Huayuan Pb-Zn orefield, reef limestone of Lower Cambrian Qingxudong Fm., black shale of Lower Cambrian Niutitang Fm. and slate of Proterozoic Banxi Group.

Deposit/Strata	Mineral/Rock	$^{206}Pb/^{204}Pb$	Mean	$^{207}Pb/^{204}Pb$	Mean	$^{208}Pb/^{204}Pb$	Mean	NO.	Source	Method
Danaopo	Sulfides	18.14–18.24	18.20	15.72–15.80	15.75	38.38–38.61	38.49	36	This paper	*In-situ*
Limei	Sphalerite and Pyrite	18.00–18.11	18.04	15.58–15.68	15.62	38.15–38.35	38.23	4	Cao et al., 2017	Bulk sulfides
Limei	Sphalerite	18.15–18.21	18.19	15.70–15.75	15.72	38.31–38.49	38.39	8	Li, 2018	
Limei	Sphalerite and Galena	17.94–18.12	18.01	15.53–15.72	15.64	38.14–38.44	38.21	5	Wei, 2017	
Shizishan	Galena and Sphalerite	18.10–18.13	18.13	15.66–15.74	15.70	38.17–38.44	38.24	4	Cai et al., 2014	
Shizishan	Galena and Sphalerite	18.01–18.14	18.07	15.62–15.68	15.66	38.11–38.30	38.24	6	Duan et al., 2014	
Naizibao	Sphalerite and Pyrite	18.05–18.12	18.08	15.63–15.69	15.66	38.26–38.35	38.30	3	Zhou et al., 2016	
Tuanjie	Sphalerite	17.92–18.83	18.25	15.55–15.64	15.60	38.09–38.24	38.15	3	Zhou et al., 2016	
Huangliandong	Sphalerite and Galena	18.02–18.16	18.11	15.58–15.73	15.69	38.12–38.51	38.33	4	Zhou et al., 2016	
Dashigou	Sphalerite and Galena	18.14–18.68	18.31	15.69–15.83	15.76	38.24–39.26	38.62	14	Li, 2018	
Laohuchong	Galena and Sphalerite	18.00–18.13	18.08	15.63–15.75	15.71	38.17–38.54	38.38	4	Wei, 2017	
Bamaozhai	Sphalerite and Galena	17.88–18.03	17.95	15.62–15.67	15.65	37.63–38.11	37.90	3	Wei, 2017	
Tudiping	Sphalerite and Galena	17.87–18.02	17.97	15.50–15.75	15.65	37.57–38.24	37.96	5	Wei, 2017	
Qingxudong Fm.	Reef limestone	18.10–18.23	18.19	15.71–15.76	15.73	38.32–38.50	38.42	6	Hu et al., 2017	Whole-rock
Qingxudong Fm.	Reef limestone	17.43–17.49	17.46	15.63–15.64	15.63	37.45–37.54	37.50	2	Cai et al., 2014	
Qingxudong Fm.	Reef limestone	17.54–17.75	17.64	15.71–15.72	15.72	37.64–37.68	37.66	2	Schneider et al., 2002	
Niutitang Fm.	Black shale	17.68–20.80	19.23	15.65–15.84	15.75	37.49–38.85	37.81	10	Chen et al., 2003	
Niutitang Fm.	Black shale	21.13	–	15.87	–	38.12	–	1	Schneider et al., 2002	
Banxi Group	Slate	16.90–18.37	17.48	15.43–15.67	15.53	37.12–40.71	38.44	14	Liu and Zhu, 1994	

Whole rock Pb isotope were corrected by mineralization age of 410 Ma (Duan et al., 2014).

the latter (Kirsch et al., 2014; Virginia and John, 2015; Wunsch et al., 2013). The Niutitang Fm. in the WHEG metallogenic belt comprises thick (>200 m) sequences of black shale, carbonates, siliceous rocks, phosphorite and clastic rocks (Jiang et al., 2008; You, 2010). Moreover, the Niutitang Fm. has considerably higher concentrations of Pb (31.4 ppm) and Zn (231.8 ppm) than most other sequences in western Hunan (Yan et al., 1997; Lei et al., 2013; Fig. 13). In particular, the black shale (Pb-Pb isochron age of 531 ± 24 Ma and Re-Os isochron age of 535 ± 11 Ma) show very high contents of Pb (76.6 ppm) and Zn (936.2 ppm) owing to the submarine hydrothermal exhalation in the early Cambrian (Jiang et al., 2006, 2008). We thus suggest that the Niutitang Fm. could have been a major metal source for the Danaopo Zn-Pb mineralization.

6.3. Metallogenic model

The Danaopo deposit has common wall-rock alteration styles (calcite, dolomite, barite, and fluorite) to typical MVT Pb-Zn deposit, simple hydrothermal mineral assemblage (pyrite, sphalerite, galena, calcite, dolomite, fluorite, and barite), single sulfur source and homogenous Pb isotope ratios, and no link to regional magmatism, which altogether suggests that the mineralization is of a sedimentary-related style. Sedimentary-diagenetic and sedimentary-reworking type Pb-Zn deposits have syngenetic sedimentation of ore-forming materials and ore-bearing rocks (Li, 1992; Luo et al., 2009; Chen et al., 2011), whereas it is precluded by the low Pb and Zn contents in the LCQF (Lei et al., 2013; Fig. 13).

The Danaopo Zn-Pb deposit is hosted in the LCQF reef limestone deposited in a carbonate platform margin (slope-facies) setting, and structurally controlled by the Huayuan-Zhangjiajie fault zone (Figs. 2 and 4). This geotectonic framework likely provided both the space for hydrothermal fluid circulation and metal precipitation, and the necessary organic matters for the TSR process. Additionally, the geological and metallogenic characteristics at the Danaopo deposit are comparable to typical MVT deposits (Table 7), except for its higher temperatures (140–328 °C) which indicate it may be an iron-rich MVT deposit (Marie et al., 2001; Xiong et al., 2019), as supported by the higher Zn/Pb ratios

Strata		Pb×10^{-6}	Zn×10^{-6}	Number	Source
East of China	carbonate rocks	8.0	18.0		Yan et al., 1997
Ordovician	O_1n	5.2	9.3	165	Lei et al., 2013
Cambrian	$\epsilon_{2-3}l$	4.8	7.4	67	
	ϵ_2g	8.3	8.8	32	
	ϵ_1q	10.1	14.9	34	
	ϵ_1s	14.5	71.3	121	
	ϵ_1n	31.4	231.8	154	
Ediacaran	Z_2dy	8.7	2.2	228	
	Z_1d	9.4	9.0	157	
Banxi Group	sandstone and slate	10	100	83	Zhou et al., 1983

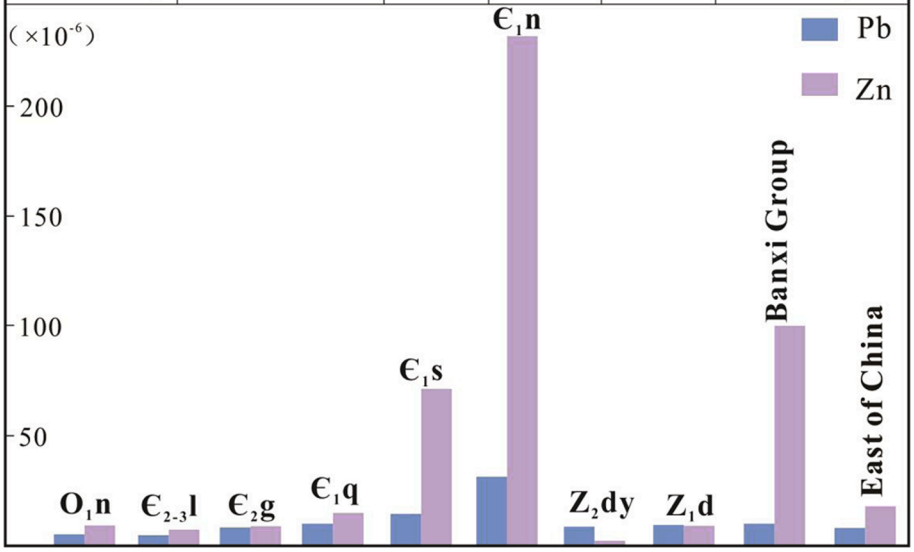

Fig. 13. Histogram of Pb-Zn contents for carbonate rocks from Eastern China (Yan et al., 1997), Banxi Gp. sandstone and slate (Zhou et al., 1983), and Ediacaran to Lower Ordovician sequences in northwestern Hunan (Lei et al., 2013).

(1.3–22.3; Table 1) and abundant pyrites in all ore stages (Fig. 7). Hence, we consider Danaopo as a MVT Zn-Pb deposit.

The Caledonian orogenic event likely promoted folding and the formation of Xuefeng Uplift, and the topographic difference (horst-graben) generated may have led to large-scale circulation and convergence of ore-bearing brine to the Huayuan district (Hu et al., 2010; Du and Xu, 2012; Wei et al., 2020). The well-mixed Pb isotopic signature may have been the result of continuous circulation of basinal brine that extracted ore-forming elements from the different strata in the district.

The Zn/Pb ratios in the Danaopo orebodies decrease from 1.3 to 22.3 with shallowing depths (Table 1), implying that the sphalerite content in the deeper level is higher than galena, and vice versa in the shallower level. Since sphalerite precipitated before galena at the Danaopo deposit, and the orebodies gradually thin out toward the margin (Fig. 4), indicating that the hydrothermal fluids first ascended from basement to ore-bearing strata, and then spread out horizontally: The ore-forming fluid was likely driven by the pressure and ascended along the Huayuan-Zhangjiajie fault zone to the LCQF. Then, the fluid may have migrated laterally and continued to extract metals from the ore-bearing strata. The acidic ore-forming fluids, low-medium temperature and medium–high salinity fluid (Liu and Zheng, 2000; Zhou et al., 2014, 2015) dissolved the carbonate wallrock, which further increased porosity of the reef limestone and thus the space for later ore precipitation. The ore precipitation was likely formed by the mixing the fluids rich in ore metals with reduced S reservoir formed by TSR of seawater sulfates (from the LCQF), facilitated by the presence of organic matters in the ore-hosting strata.

7. Conclusions

(1) Sulfur isotope compositions of sulfates and sulfides at the Danaopo deposit reveal that the sulfur source was originated from TSR of marine sulfates in the ore-bearing strata, which occurred at around 147–300 °C.
(2) Sulfide Pb isotope compositions suggest well-mixing of multiple Pb sources, including mainly the LCNF black shale with minor contribution from the Proterozoic Banxi Gp. metamorphic basement rocks, and the LCQF reef limestone.
(3) Danaopo is best classified as a MVT Zn-Pb deposit, and the ore deposition was likely triggered by the mixing of ore-forming fluid with reduced sulfur reservoir during the Early Devonian orogenic event (~410 Ma).

Declaration of Competing Interest

The authors declare that they have no known competing financial interests or personal relationships that could have appeared to influence the work reported in this paper.

Table 7
Typical geological characteristics of MVT deposit and Danaopo Zn-Pb deposit.

Characteristics	Typical MVT Pb-Zn deposit	Danaopo Zn-Pb deposit
Tonnages and grades	Single orebodies < 1 Mt, av. Pb + Zn < 10 wt%	~4.57 Mt Pb + Zn reserves with av. 2.58 wt% Zn and 0.48 wt% Pb
Mineralization Depths	< 1500 m	200–400 m
Mineralization ages	Epigenetic, Proterozoic to Cretaceous	Epigenetic, Late Silurian to Early Devonian (~410 Ma)
Tectonic setting	Carbonate platform, Foreland basin of passive continental margin	Slope facies of carbonate platform margin
Relationship with magmatism	Little relationship with igneous activities	Irrelevant with regional magmatism
Ore-bearing rocks	Cambrian to Carboniferous carbonate rocks	Lower Cambrian Qingxudong Fm. reef limestone
Ore-controlling factors	Faults, folds and lithology	Huayuan-Zhangjiajie fault belt and algal reef zone
Orebodies occurrences	Layered, stratoid, veined and lenticular	Stratoid and lenticular
Wall-rock alterations	Dolomitiz-, calcitiz-, baritiz-, fluoritiz- and silicific-ation	Calcitiz-, dolomitiz-, baritiz- and fluoritiz-ation
Ore structures	Disseminated, massive, fine-granular and colloidal	Porphyritic veined, piebald (similar to disseminated) and massive
Ore textures	Colloidal and skeleton coarse-crystalline	subhedral to anhedral granular, metasomatic, poikilitic and interstitial
Ore minerals compositions	Sphalerite, galena, pyrite and marcasite	Sphalerite, galena, pyrite
Gangue minerals	dolomite, calcite, barite, fluorite, quartz and bitumen	Calcite, dolomite, barite, fluorite (and bitumen)
Associated metal (s)	Ag	Cd and Ag
Temperature and salinity	50–250 °C, 10–30 wt% NaCl equiv.	140–328 °C, 4.5–21.4 wt% NaCl equiv.
Organic matter	Bitumen and hydrocarbon inclusions	CH_4-bearing fluid inclusions (and bitumen)
Sulfur source(s)	Seawater sulfate ($\delta^{34}S$: +10 to +35‰)	Seawater sulfate in the ore-bearing strata ($\delta^{34}S$: +23.5 to +35.5‰)
Metals source(s)	Basements and sediments	Metamorphic basement of the Proterozoic Banxi Group + black shale of the LCNF (+reef limestone of the LCQF).
Precipitation mechanism	Reduced S, Sulfate reduction or mixing of reduced S and metals	Mixing of reduced S and metals
References	Leach et al. (2005), Leach et al. (2010), Zhou et al. (2018a), Xiong et al. (2019)	Yang and Lao (2007), Yu et al. (2014), Duan et al. (2014), Zhou et al. (2015), This study

Acknowledgements

This research was supported by the National Natural Science Foundation of China (U1812402 and 41673056). We thank Drs. Kaiyun Chen and Zhian Bao for helping with the S-Pb isotope analyses. We are grateful to Team 405 Hunan BGMR for granting mine access and sampling.

References

Bao, Z.A., Chen, L., Zong, C.L., Yuan, H.L., Chen, K.Y., Dai, M.N., 2017a. Development of pressed sulfide powder tablets for *in situ* sulfur and lead isotope measurement using LA-MC -ICP-MS. Int. J. Mass Spectrom. 421, 255–262.
Bao, Z.W., Li, Q., Wang, Y.C., 2017b. Metal source of giant Huize Zn-Pb deposit in SW China: New constraints from *in situ* Pb isotopic compositions of galena. Ore Geol. Rev. 91, 824–836.
Basuki, N.I., Taylor, B.E., Spooner, E.T.C., 2008. Sulfur isotope evidence for thermochemical reduction of dissolved sulfate in Mississippi valley type zinc-lead mineralization, Bongara area, northern Peru. Econ. Geol. 103, 183–799.
Bendall, C., Lahaye, Y., Fiebig, J., Weyer, S., 2006. *In situ* sulfur isotope analysis by laser ablation MC-ICPMS. Appl. Geochem. 21, 782–787.
Cai, Y.X., Yang, H.M., Duan, R.C., Lu, S.S., Zhang, L.G., Liu, Z.P., Qiu, X.F., 2014. Fluid inclusions and S, Pb, C isotope geochemistry of Pb-Zn deposits hosted by Lower Cambrian in western Hunan-eastern Guizhou area. Geosci. 28, 29–41 (in Chinese with English abstract).
Canals, A., Cardellach, E., 1997. Ore lead and sulfur isotope pattern from the low-temperature veins of the Catalonian Coastal Ranges (NE Spain). Miner. Deposita 32, 243–249.
Cao, L., Duan, Q.F., Peng, S.G., Zhou, Y., Li, K., Gan, J.M., 2017. Sources of metallogenic materials of lead-zinc deposits in western Hunan Province: Evidence from S and Pb isotopes. Geol. Bull. China 36, 834–845 (in Chinese with English abstract).
Carr, G.R., Dean, J.A., Suppel, D.W., Heithersay, P.S., 1995. Precise lead isotope fingerprinting of hydrothermal activity associated with Ordovician to Carboniferous metallogenic events in the Lachlan fold belt of New South Wales. Econ. Geol. 90, 1467–1505.
Chaussidon, M., Albarède, F., Sheppard, S.M.F., 1989. Sulfur isotope variations in the mantle from ion microprobe analyses of micro-sulfide inclusions. Earth Planet. Sci. Lett. 92, 144–156.
Chen, J., Wang, H.N., 2004. In: Geochemistry. Science Press, Beijing, pp. 129–140 (in Chinese).
Chen, L., Chen, K.Y., Bao, Z.A., Liang, P., Sun, T.T., Yuan, H.L., 2017. Preparation of standards for *in situ* sulfur isotope measurement in sulfides using femtosecond laser ablation MC-ICP-MS. J. Anal. At. Spectrom. 32, 107–116.
Chen, M.H., Hu, X.Z., Bao, Z.X., Bao, J.M., 2011. Geological features and metallogenesis of the Yutang Pb-Zn ore concentration belt in Hunan Province. Geol. Explor. 47 (2), 251–260 (in Chinese with English abstract).
Chen, Y.P., Xiang, N., Tang, Q., Ma, C.C., 2018. Geological characteristics and metallogenic geological conditions of Danaopo Zn-Pb deposit in western Hunan. Miner. Explor. 9, 1127–1133 (in Chinese with English abstract).
Chen, Y.Q., Jiang, S.Y., Ling, H.F., Feng, H.Z., Yang, J.H., Chen, J.H., 2003. Pb-Pb isotope dating of black shales from the Lower Cambrian Niutitang Formation, Guizhou Province, South China. Prog. Nat. Sci. 13, 771–776.
Chu, X.L., Chen, J.S., Wang, S.X., 1984. Several diagrams of sulfur isotope evolution in equilibrium with hydrothermal system. Sci. Geol. Sinica 2, 186–200 (in Chinese with English abstract).
Claypool, G.E., Holser, W.T., Kaplan, I.R., Sakai, H., Zak, I., 1980. The age curves of sulfur and oxygen isotopes in marine sulfate and their mutual interpretation. Chem. Geol. 28, 199–260.
Cunha, I.A., Misi, A., Babinski, M., Iyer, S.S.S., 2007. Lead isotope constraints on the genesis of Pb-Zn deposits in the Neoproterozoic Vazante Group, Minas Gerais, Brazil. Gondwana Res. 11, 382–395.
Ding, T., Ma, D.S., Lu, J.J., Zhang, R.Q., Zhang, S.T., 2016. S, Pb, and Sr isotope geochemistry and genesis of Pb-Zn mineralization in the Huangshaping polymetallic ore deposit of southern Hunan Province, China. Ore Geol. Rev. 77, 117–132.
Du, G.M., Cai, H., Mei, Y.P., 2012. Application of Rb–Sr isochron dating method in sphalerite of sulfide deposit—A case study from Dagoudong Pb-Zn deposit in Xinhuang, western Hunan Province. Geol. Miner. Resour. South China 28, 175–180 (in Chinese with English abstract).
Duan, Q.F., Cao, L., Zeng, J.K., Zhou, Y., Tang, Z.Y., Li, K., 2014. Rb-Sr dating of sphalerites from Shizishan Pb-Zn deposit and its geological significance in Huayuan Ore Concentration Area, Western Hunan. Earth Sci.-J. China Univ. Geosci. 39, 977–999 (in Chinese with English abstract).
Du, Y.S., Xu, J.Y., 2012. A preliminary study on Caledonian event in South China. Geol. Sci. Technol. Inf. 31, 43–49 (in Chinese with English abstract).
Fan, Z.Q., Yu, M.S., Zhong, T.S., 1986. Tentative investigation of the origin and geological features of layered barite deposit from pneumato-hydrothermal sedimentary genesis in Gongxi, western Hunan Province. Miner. Rocks 6, 65–75 (in Chinese with English abstract).
Feng, X.Y., Meng, X.G., Shao, Z.G., Wang, J.P., Zhu, D.G., 2003. A preliminary discussion on features and dynamics of sequence deformation in South China and neighboring areas. Acta Geosci. Sinica 24, 115–120 (in Chinese with English abstract).
Fu, S.Y., 2011. Discussion on the formation rules of high-grade Pb-Zn deposit in western Hunan Province. Nonferrous Met. Eng. 63, 27–35 (in Chinese with English abstract).
Hu, S.Q., Zhu, G., Zhang, B.L., Zhang, L., 2010. K-Ar geochronology of the caledonian event in the Xuefeng uplift. Geol. Rev. 56, 490–500 (in Chinese with English abstract).
Hu, T.P., Wang, M.F., Ding, Z.J., He, M.C., Wang, Y.B., Guo, X.N., 2017. C, O, S and Pb isotopic characteristics and sources of metallogenic materials of Limei Pb-Zn deposit in Huayuan county, western Hunan province. Miner. Deposits 36, 623–642 (in Chinese with English abstract).
Ikehata, K., Notsub, K., Hiratac, T., 2008. *In situ* determination of Cu isotope ratios in copper-rich materials by NIR femtosecond LA-MC-ICP-MS. J. Anal. At. Spectrom. 23, 1003–1008.
Jiang, S.Y., Chen, Y.Q., Ling, H.F., Yang, J.H., Feng, H.Z., Ni, P., 2006. Trace- and rare-earth element geochemistry and Pb-Pb dating of black shales and intercalated Ni-Mo-PGE-Au sulfide ores in Lower Cambrian strata, Yangtze Platform, South China. Miner. Depos. 41, 453–467.
Jiang, S.Y., Ling, H.F., Zhao, K.D., Zhu, M.Y., Yang, J.H., Chen, Y.Q., 2008. A discussion on Mo isotopic compositions of black shale and Ni-Mo sulfide bed in the early Cambrian Niutitang Formation in south China. Acta Petrol. et Mineral. 27, 341–345 (in Chinese with English abstract).
Jørgenson, B.B., Isaksen, M.F., Jannasch, H.W., 1992. Bacterial sulfate reduction above 100 °C in deep sea hydrothermal vent sediments. Science 258, 1756–1757.
Jones, H.D., Kesler, S.E., 1997. Sulfur Isotope Geochemistry of Southern Appalachian Mississippi Valley-Type Deposits. Econ. Geol. 91, 355–367.
Kirsch, K., Navarre-Sitchler, A.K., Wunsch, A., McCray, J.E., 2014. Metal release from sandstones under experimentally and numerically simulated CO_2 leakage conditions. Environ. Sci. Technol. 48, 1436–1442.

Kuang, W.L., Xiang, S.C., Xiao, W.Z., Chen, W., Yang, S.X., Yu, P.R., Chen, N.S., 2015. Metallogenic geological characteristics and genesis of lead-zinc deposits in northwestern Hunan. Miner. Deposita 34, 1072–1082 (in Chinese with English abstract).
Leach, D.L., Sangster, D.F., Kelley, K.D., Large, R.R., Garven, G., Allen, C.R., Gutzmer, J., Walters, S., 2005. Sediment-hosted lead-zinc deposits: a global perspective. Econ. Geol. 100, 561–607.
Leach, D.L., Bradley, D.C., Huston, D., Pisarevsky, S.A., Taylor, R.D., Gardoll, S.J., 2010. Sediment-hosted lead-zinc deposits in earth history. Econ. Geol. 105, 593–625.
Leach, D.L., 2014. Evaporites and Mississippi Valley-type Zn-Pb-Ag deposits: an evolving perspective. Acta Geol. Sin. 88, 174–175.
Lei, Y.J., Dai, P.Y., Duan, Q.F., Liu, A.S., Tao, M., 2013. Constraints of lead-zinc source bed to lead-zinc deposits in western Hubei to northwestern Hunan. J. Guilin Univ. Technol. 33, 1–6 (in Chinese with English abstract).
Li, K., Liu, K., Tang, Z.Y., Duan, Q.F., 2013. Characteristics of zinc geochemical blocks and assessment of zinc resource potential in western Hunan and eastern Guizhou Province. Geol. China 40, 1270–1277 (in Chinese with English abstract).
Li, K., 2018. Metallogenic model and prediction of the carbonate-hosted Pb-Zn deposits in western Hunan and eastern Guizhou province, south China (PH.D. thesis). China University of Geosciences (Wuhan), pp. 2–128 (in Chinese with English abstract).
Li, M.L., Liu, S.A., Xue, C.J., Li, D., 2019. Zinc, Cadmium and sulfur isotope fractionation in a supergiant MVT deposit with bacteria. Geochim. Cosmochim. Acta 265 (2019), 1–18.
Li, Z.F., 1992. S and Pb isotope from feature of Pb-Zn ore-belt in the border of Guizhou-Hunan Province, China. Geol. Guizhou 9 (3), 246–254 (in Chinese with English abstract).
Liu, H.C., Zhu, B.Q., 1994. Study on the age of Banxi Group and Lengjiaxi Group in western Hunan. Chin. Sci. Bull. 39, 148–150 (in Chinese).
Liu, W.J., Zheng, R.C., Li, Y.L., Gao, L., 1999b. Study of bitumen in the Huayuan lead-zinc deposit: organic geochemistry study of MVT lead-zinc deposit. Acta Sedimentol. Sin. 17, 19–23 (in Chinese with English abstract).
Liu, W.J., Zheng, R.C., 1999a. Research of fluid inclusion gas composition in Huayuan lead-zinc deposits: Organic-mineralization study of MVT lead-zinc deposits(II). Acta Sedimentol. Sin. 17, 608–614 (in Chinese with English abstract).
Liu, W.J., Lu, J.L., 2000. Characteristics of organic geochemistry of Lower Cambrian in western Hunan: organic-mineralization study on MVT lead-zinc ore deposits. Acta Sedimentol. Sin. 18, 290–296 (in Chinese with English abstract).
Liu, W.J., Zheng, R.C., 2000. Characteristics and movement of ore-forming fluids in the Huayuan lead-zinc deposit. Miner. Deposita 19, 173–181.
Liu, Y.J., 2017. The organic geochemical characteristics research of the lower Cambrian Niutitang black shale in northwestern Hunan (Master's thesis). China Univ. Petrol. 1–50 (in Chinese with English abstract).
Luo, K., Zhou, J.X., Huang, Z.L., Wang, X.C., Wilde, S.A., Zhou, W., Tian, L., 2019. New insights into the origin of early Cambrian carbonate-hosted Pb-Zn deposits in South China: a case study of the Maliping Pb-Zn deposit. Gondwana Res. 70, 88–103.
Luo, K., Zhou, J.X., Huang, Z.L., Caulfield, J., Zhao, J.X., Feng, Y.X., Ouyang, H., 2020. New insights into the evolution of Mississippi Valley-Type hydrothermal system: a case study of the Wusihe Pb-Zn deposit, South China, using quartz in-situ trace elements and sulfides *in situ* S-Pb isotopes. Am. Miner. 105 (1), 35–51.
Luo, W., Yin, Z., Kong, L., Dai, T.G., 2009. Discussion on the geological features and genesis of the Limei Pb-Zn ore concentration belt in northwestern Hunan Province. Geol. Surv. Res. 33, 194–202 (in Chinese with English abstract).
Machel, H.G., 1989. Relationships between sulfate reduction and oxidation of organic compounds to carbonate diagenesis, hydrocarbon accumulations, salt domes, and metal sulfide deposits. Carbonates Evaporites 4, 137–151.
Machel, H.G., Krouse, H.R., Sassen, R., 1995. Products and distinguishing criteria of bacterial and thermo-chemical sulfate reduction. Appl. Geochem. 10, 373–389.
Mao, D.L., 2016. Geological characteristics and genesis of the Danaopo Zn-Pb deposit in Huayuan County, Hunan Province. Modern Mining 562, 90–97 (in Chinese with English abstract).
Marie, J.S., Kesler, S.E., Allen, C.R., 2001. Origin of iron-rich Mississippi Valley-type deposits. Geology 29 (1), 59–62.
Ohmoto, H., 1972. Systematics of sulfur and carbon isotopes in hydrothermal ore deposits. Econ. Geol. 67, 551–578.
Ohmoto, H., Rye, R.O., 1979. Isotopes of sulfur and carbon. In: Barnes, H.L. (Ed.), Geochemistry of Hydrothermal Ore Deposits. Wiley-Interscience, New York, pp. 509–567.
Peevlera, J., Fayekb, M., Misra, K.C., Riciputi, L.R., 2003. Sulfur isotope microanalysis of sphalerite by SIMS: constraints on the genesis of Mississippi valley-type mineralization, from the Mascot-Jefferson City district, East Tennessee. J. Geochem. Explor. 80, 277–296.
Rees, C.E., 1973. A steady-state model for sulfur isotope fractionation in bacterial reduction processes. Geochim. Cosmochim. Acta 37, 1141–1162.
Rye, R.O., Ohmoto, H., 1974. Sulfur and carbon isotopes and ore genesis: a review. Econ. Geol. 69, 826–842.
Rye, R.O., Hall, W.E., Ohmoto, H., 1974. Carbon, hydrogen, oxygen and sulfur isotope study of Darwin lead-silver-zinc deposit, southern California. Econ. Geol. 69, 468–481.
Schneider, J., Lapponi, F., Boni, M., Bechstadt, T., 2002. Carbonate-hosted zinc-lead deposits in the Lower Cambrian of Hunan, South China: a radiogenic (Pb, Sr) isotope study. Econ. Geol. 97, 1815–1827.
Seal, R.R., Alpers, C.N., Rye, R.O., 2000. Stable isotope systematics of sulfate minerals. Rev. Mineral. Geochem. 40, 541–602.
Seal, R.R., 2006. Sulfur isotope geochemistry of sulfide minerals. Rev. Mineral. Geochem. 61, 633–677.
Shu, J.W., 1983. Preliminary discussion on the origin of lead and zinc sulfide deposit in Yutang area. Geotectonica et Metallogenia 7, 309–320 (in Chinese with English abstract).
Sim, M.S., Bosak, T., Ono, S., 2011. Large sulfur isotope fractionation does not require disproportionation. Science 333, 74–77.
Souders, A.K., Sylvester, P.J., 2010. Accuracy and precision of non-matrix-matched calibration for lead isotope ratio measurements of lead-poor minerals by LA-MC-ICPMS. J. Anal. At. Spectrom. 25, 975–988.
Tan, J.J., Liu, C.P., Yang, H.M., Cai, Y.X., Lu, S.S., 2018. Geochronology and ore-forming material source constraints for Rouxianshan Pb-Zn deposit in Huayuan ore concentration area, western Hunan. Earth Sci. 43, 2438–2448 (in Chinese with English abstract).
Tan, S.C., Zhou, J.X., Li, B., Zhao, J.X., 2017. *In situ* Pb and bulk Sr isotope analysis of the Yinchanggou Pb-Zn deposit in Sichuan Province (SW China): Constraints on the origin and evolution of hydrothermal fluids. Ore Geol. Rev. 91, 432–443.
Tang, Z.Y., Deng, F., Li, K., Wang, G.Q., Duan, Q.F., Zou, X.W., Zhao, W.Q., Jin, S.C., 2012. Sedimentary Sequence of the Lower Cambrian Qingxudong Formation in the western Hunan and eastern Guizhou provinces and its constrains on lead-zinc mineralization. Geotectonica et Metallogenia 36, 111–117 (in Chinese with English abstract).
Tang, Z.Y., Deng, F., Li, K., Zhao, W.Q., Jin, S.C., 2013. Lithofacies paleogeography of the Qingxudong epoch, Duyun stage, Cambrian Period and its relationship to lead-zinc deposits in western Hunan and eastern Guizhou Provinces. Geol. Explor. 49, 19–27 (in Chinese with English abstract).
Virginia, M., John, P.K., 2015. Carbon dioxide-brine-rock interactions in a carbonate reservoir capped by shale: experimental insights regarding the evolution of trace metals. Geochim. Cosmochim. Acta 168, 22–42.
Wang, L.J., Mi, M., Zhou, J.X., Luo, K., 2018. New constraints on the origin of the Maozu carbonate-hosted epigenetic Zn-Pb deposit in NE Yunnan Province, SW China. Ore Geol. Rev. 101, 578–594.
Wei, H.T., 2017. Mineralization of the Huayuan Pb-Zn orefield, western Hunan (PH.D. thesis). Central South University, pp. 7–9 (in Chinese with English abstract).
Wei, H.T., Shao, Y.J., Xiong, Y.Q., Liu, W., Kong, H., Li, J., Sui, Z.H., 2017. Metallogenic model of Huayuan Pb-Zn ore field in the western Hunan Province, South China. J. Cent. South Univ. (Sci. Technol.) 48, 2402–2413 (in Chinese with English abstract).
Wei, H.T., Shao, Y.J., Xiao, K.Y., Kong, H., Zhang, S., Wang, K., Li, Q., Chen, B.H., Xiang, J., Wen, C.H., 2020. Modeling-based mineral system approach to prospectivity mapping of stratabound hydrothermal deposits: A case study of MVT Pb-Zn deposits in the Huayuan area, northwestern Hunan Province, China. Ore Geol. Rev. 120, 1–12.
Worden, R.H., Smalley, P.C., Oxtoby, N.H., 1995. Gas souring by the thermo chemical sulfate reduction at 140 °C. AAPG Bull. 79, 854–863.
Wunsch, A., Navarre-Sitchler, A.K., Moore, J., McCray, J.E., 2013. Metal release from limestones at high partial-pressures of CO_2. Chem. Geol. 363, 40–55.
Xiong, S.F., Jiang, S.Y., Ma, Y., Liu, T., Zhao, K.D., Jiang, M.R., Zhao, H.D., 2019. Ore genesis of Kongxigou and Nanmushu Zn-Pb deposits hosted in Neoproterozoic carbonates, Yangtze Block, SW China: Constraints from sulfide chemistry, fluid inclusion, and *in situ* S-Pb isotope analyses. Precambr. Res. 333, 1–24.
Yan, M.C., Chi, Q.H., Gu, T.X., Wang, C.S., 1997. Chemical compositions of continental crust and rocks in eastern China. Geophys. Geochem. Explor. 21, 451–459 (in Chinese with English abstract).
Yang, H.M., Liu, C.P., Duan, R.C., Gu, X.M., Lu, S.S., Tan, J.J., Cai, Y.X., Zhang, L.G., Qiu, X.F., 2015. Rb-Sr and Sm-Nd isochron ages of Bokouchang Pb-Zn Deposit in Tongren, Guizhou Province and their geological implication. Geotectonica et Metallogenia 39, 855–865 (in Chinese with English abstract).
Yang, S.X., Lao, K.T., 2007. Geological characteristics and ore indicators of lead-zinc deposits in northwestern Hunan, China. Geol. Bull. China 26, 899–908 (in Chinese with English abstract).
You, X.J., 2010. Research on the Ni-Mo-V deposits in Lower Cambrian black rock series in Western Hunan (PH.D. thesis). Central South University, pp. 2–48 (in Chinese with English abstract).
Yuan, H.L., Yin, C., Liu, X., Chen, K.Y., Bao, Z.A., Zong, C.L., Dai, M.N., Lai, S.C., Wang, R., Jiang, S.Y., 2015. High precision in-situ Pb isotopic analysis of sulfide minerals by femtosecond laser ablation multi-collector inductively coupled plasma mass spectrometry. Sci. China-Earth Sci. 58, 1713–1721.
Yuan, H.L., Liu, X., Chen, L., Bao, Z.A., Chen, K.Y., Zong, C.L., Li, X.C., Qiu, W.H., 2018. Simultaneous measurement of sulfur and lead isotopes in sulfides using nanosecond laser ablation coupled with two multi-collector inductively coupled plasma mass spectrometers. J. Asian Earth Sci. 154, 386–396.
Yu, P.R., Deng, W.D., Zeng, J.K., Mao, D.L., 2014. The general survey report of Danaopo Zn-Pb deposit in Huayuan orefield, western Hunan Province. 405 Team of Hunan Geological and Mineral Bureau, pp. 5–119 (in Chinese).
Zartman, R.E., Doe, B.R., 1981. Plumbotectonics-the model. Tectonophysics 75, 135–162.
Zhao, S., Pan, W., Yang, S.T., Yin, T.L., Jiang, T.R., Tian, J.J., Chen, L., Qin, Z.G., 2016. Geological characteristics and genesis of lead-zinc deposits by Lower Cambrian in western Hunan-northeastern Guizhou area, China. Guizhou Geol. 33, 257–263 (in Chinese with English abstract).
Zhou, H.D., Shao, Y.J., Ye, Z., Wei, H.T., 2015. Study on fluid inclusions of Danaopo lead-zinc deposit in Huayuan County, western Hunan Province. Acta Mineral. Sinica, 652 (in Chinese).
Zhou, J.X., Huang, Z.L., Yan, Z.F., 2013. The origin of the Maozu carbonate-hosted Pb-Zn deposit, southwest China: constrained by C-O-S-Pb isotopic compositions and Sm-Nd isotopic age. J. Asian Earth Sci. 73, 39–47.

Zhou, J.X., Luo, K., Wang, X.C., Wilde, S.A., Wu, T., Huang, Z.L., Cui, Y.L., Zhao, J.X., 2018a. Ore genesis of the Fule Pb-Zn deposit and its relationship with the Emeishan Large Igneous Province: Evidence from mineralogy, bulk C-O-S and *in situ* S-Pb isotopes. Gondwana Res. 54, 161–179.

Zhou, J.X., Xiang, Z.Z., Zhou, M.F., Feng, Y.X., Luo, K., Huang, Z.L., Wu, T., 2018b. The giant Upper Yangtze Pb-Zn province in SW China: Reviews, new advances and a new genetic model. J. Asian Earth Sci. 154, 280–315.

Zhou, Y., Duan, Q.F., Tang, J.X., Cao, L., Li, F., Huang, H.L., Gan, J.M., 2014. The large-scale low-temperature mineralization of lead-zinc deposits in western Hunan: evidence from fluid inclusions. Geol. Explor. 50, 515–532 (in Chinese with English abstract).

Zhou, Y., Duan, Q.F., Chen, Y.C., Tang, J.X., Cao, L., Peng, S.G., Gan, J.M., 2016. C, O, H, S, Pb and Sr isotope constraints on the metals sources of Huayuan Pb-Zn deposit in western Hunan Province. Acta Geol. Sinica 90, 2786–2802 (in Chinese with English abstract).

Zhou, Y., Duan, Q.F., Tang, J.X., Cao, L., Peng, S.G., Gan, J.M., 2017. Carbon, hydrogen and oxygen isotopes of the Huayuan Pb-Zn ore deposit in western Hunan Province and their implications for the source of ore-forming fluid. Geol. Bull. China 36, 823–833 (in Chinese with English abstract).

Zhou, Z.D., Wang, R.M., Zhuang, R.L., Lao, K.T., 1983. The genesis of Yutang Pb-Zn deposit in Huayuan orefield, Hunan Province. J. Chengdu Inst. Geol. 3, 1–15 (in Chinese with English abstract).